BNL-212084-2019-JAAM

X-Ray Scattering and Coarse-Grained Simulations for Clustering and Interactions of Monoclonal Antibodies at High Concentrations

B. Dear, D. Nykypanchuk

To be published in "The Journal of Physical Chemistry B"

May 2019

Center for Functional Nanomaterials

Brookhaven National Laboratory

U.S. Department of Energy

USDOE Office of Science (SC), Basic Energy Sciences (BES) (SC-22)

Notice: This manuscript has been authored by employees of Brookhaven Science Associates, LLC under Contract No. DE-SC0012704 with the U.S. Department of Energy. The publisher by accepting the manuscript for publication acknowledges that the United States Government retains a non-exclusive, paid-up, irrevocable, world-wide license to publish or reproduce the published form of this manuscript, or allow others to do so, for United States Government purposes.

DISCLAIMER

This report was prepared as an account of work sponsored by an agency of the United States Government. Neither the United States Government nor any agency thereof, nor any of their employees, nor any of their contractors, subcontractors, or their employees, makes any warranty, express or implied, or assumes any legal liability or responsibility for the accuracy, completeness, or any third party's use or the results of such use of any information, apparatus, product, or process disclosed, or represents that its use would not infringe privately owned rights. Reference herein to any specific commercial product, process, or service by trade name, trademark, manufacturer, or otherwise, does not necessarily constitute or imply its endorsement, recommendation, or favoring by the United States Government or any agency thereof or its contractors or subcontractors. The views and opinions of authors expressed herein do not necessarily state or reflect those of the United States Government or any agency thereof.

X-Ray Scattering and Coarse-Grained Simulations for Clustering and Interactions of Monoclonal Antibodies at High Concentrations

Barton J. Dear[a], Jonathan A. Bollinger[a,b], Amjad Chowdhury[a], Jessica J. Hung[a], Logan R. Wilks[a], Carl A. Karouta[a], Kishan Ramachandran[a], Tony Y. Shay[a], Maria P. Nieto[a], Ayush Sharma[a], Jason K. Cheung[c], Dmytro Nykypanchuk[d], P. Douglas Godfrin[e], Keith P. Johnston*[a] and Thomas M. Truskett*[a,f]

a. McKetta Department of Chemical Engineering, The University of Texas at Austin, Austin, TX 78712, United States
b. Center for Integrated Nanotechnologies, Sandia National Laboratories, Albuquerque, NM 87185, United States
c. Biophysical and Biochemical Characterization, Sterile Formulation Sciences, Merck & Co., Inc., Kenilworth, NJ 07033 USA
d. Center for Functional Nanomaterials, Brookhaven National Laboratory, Upton, NY 11973, United States
e. Department of Chemical Engineering, Massachusetts Institute of Technology, Cambridge, MA 02139, United States
f. Department of Physics, The University of Texas at Austin, Austin, TX 78712, United States

Corresponding authors:

Keith P. Johnston – Phone: (512) 471-4617 email: johnston@che.utexas.edu

Thomas M. Truskett – Phone: (512) 471-6308 email: truskett@che.utexas.edu

Abstract

Attractive protein-protein interactions (PPI) in concentrated monoclonal antibody (mAb) solutions may lead to reversible oligomers (clusters) that impact colloidal stability and viscosity. Herein, the PPI are tuned for two mAbs via the addition of arginine (Arg), NaCl, or $ZnSO_4$ as characterized by the structure factor ($S_{eff}(q)$) with small angle x-ray scattering (SAXS). The SAXS data are fit with molecular dynamics simulations by placing a physically relevant short-ranged attractive interaction on selected beads in coarse-grained 12 bead models of the mAb shape. The optimized 12-bead models are then used to differentiate key microstructural properties, including center of mass radial distribution functions ($g_{COM}(r)$), coordination numbers and cluster size distributions (CSD). The addition of co-solutes results in more attractive $S_{eff}(q)$ relative to the no co-solute control for all systems tested, with the most attractive systems showing an upturn at low q. Only the All1 model with an attractive site in each Fab and Fc region (possessing Fab-Fab, Fab-Fc and Fc-Fc interactions) can reproduce this upturn, and the corresponding CSDs show the presence of larger clusters compared to the control. In general, for models with similar net attractions, i.e., second osmotic virial coefficients, the size of the clusters increases as the attraction is concentrated on a smaller number of evenly distributed beads. The cluster size distributions from simulations are used to improve the understanding and prediction of experimental viscosities. The ability to discriminate between models with bead interactions at particular Fab and Fc bead sites from SAXS simulations, and to provide real space properties (CSD and $g_{COM}(r)$), will be of interest in engineering protein sequence and formulating protein solutions for weak PPI to minimize aggregation and viscosities.

Introduction

Despite the large emphasis on the discovery and development of monoclonal antibodies (mAbs) for treating a wide variety of diseases, including autoimmune diseases and cancer,[1-2] it remains challenging to form stable solutions at efficacious concentrations (from 100 to 300+ mg/ml) with viscosities suitable for subcutaneous administration ($\leq$ 20 cP).[3-5] At these elevated concentrations, with an average separation distance between mAbs on the order of a few nanometers, protein-protein interactions (PPI) have a significant influence on solution properties. Types of PPI include steric repulsions, short-ranged van der Waals (vdW) and hydrophobic attractions, long-ranged electrostatic repulsions, and short-ranged local anisotropic attractions between small numbers of amino acids (defined here to include charge-dipole, dipole-dipole and hydrogen bonding interactions).[6-14] The relationship(s) between these classes of PPI and reversible oligomer or cluster formation in mAbs is highly complex and of great current interest for understanding corresponding solution viscosities[9-10, 12, 15-18] and the formation of irreversible aggregates.[18-21]

To facilitate the discovery and development of mAbs, several studies have attempted to predict mAb solution viscosities from their amino acid sequence with semi-empirical models.[22-25] These studies find that mAbs with charge anisotropy, either between the antigen binding fragment (Fab) and the crystallizable fragment (Fc),[23-25] or between the heavy and light chain of the Fab,[22, 25] are prone to elevated viscosities, as are mAbs with higher hydrophobicity.[22, 25] However, each of these statistical models requires a complex combination of descriptors and has only been tested in a single formulation for each mAb. In contrast, within various experimental studies, formulation has been used to lower mAb viscosities by adjusting pH,[26-27] ionic strength,[26, 28-30] and/or via the addition of co-solutes such as carbohydrates,[31-33] hydrophobic ions,[34-35] and amino acids and their derivatives.[27, 35-44] Given the large combinatorial space of formulation options, it would be desirable to develop a more fundamental understanding of the relationship between solution conditions, PPI, and viscosity for various classes of mAbs.

Many studies have focused on predicting mAb solution viscosities at high concentrations based on estimates of PPI strengths measured at low concentrations, but with limited success. The emphasis has been on second virial coefficients (B_{22}) measured via static light scattering (SLS) and the diffusion interaction parameter (k_D) measured via dynamic light scattering (DLS) as they are straightforward to determine and require only small amounts of protein.[18, 27, 45] Qualitative correlations between solution viscosities and B_{22} or k_D have been demonstrated for a series of mAbs.[18, 45] When restricted to a single

mAb, quantitative correlations with respect to varying pH and co-solutes over a narrow range in ionic strength have been found.[27] High concentration viscosities have also been correlated to the mAb apparent maximum dimension, $D_{max,app}$ and apparent radius of gyration, $R_{g,app}$, from small angle x-ray scattering (SAXS) intensity curves. This approach has been used at either intermediate concentrations (60 mg/ml)[40] or at low concentration and low temperature (15 mg/ml and 5°C to enhance PPI)[41] across various mAbs in high ionic strength solutions. However, these techniques do not yield any knowledge about high concentration microstructure or PPI and further work is required to validate their general applicability.

Although developing reliable empirical relations between low-concentration measurements and viscosity remains desirable, a complementary set of studies have focused on using theoretical approaches to describe viscosity data in terms of PPI strength and self-association. For example, the Ross-Minton (RM) hard quasi-spherical model,[46] particularly in its linearized form,[20] may be used to qualitatively identify the concentration-dependent formation of clusters, which decrease the packing efficiency and raise the viscosity.[20, 27, 47] A polymer entanglement model has been developed to relate cluster size and viscosity to a Fab-Fab binding energy, though the cluster sizes for mAbs tend to involve relatively less entanglement than large-molecular-weight polymers.[48] Similarly, one recent approach applies Wertheim's thermodynamic perturbation theory[49] to predict cluster size distributions based on a seven bead mAb model that was used to fit experimental viscosity data across several formulations, concentrations, and temperatures.

Despite these developments, it remains of great interest to characterize PPI and solution structure at high concentrations, and recently considerable gains have been made by combining static scattering techniques, including SAXS,[50-52] small angle neutron scattering (SANS),[29, 53-55] and SLS,[7-8, 17, 47, 56-60] with modeling approaches based on liquid-state theory and molecular simulations. However, to maximize the information gained from SLS, SAXS, and SANS experiments at high-concentration, it is critical to develop and validate models for mAbs that can be directly (and accurately) parameterized to fit scattering data. This approach provides PPI estimates and microscopic insight into mAb self-association. For example, the relatively high viscosity of one widely studied mAb, GmAb1, was found attributable to high charge anisotropy based on its sequence, with negatively charged sites in the complementary determining regions (CDR) of the Fab, and mostly positive charges elsewhere, particularly in the Fc.[13] In SANS experiments of GmAb1, the structure factor, S(q), which probes structural correlations driven by intermolecular interactions, indicates strongly attractive PPI. As the

ionic strength is increased, anisotropic electrostatic interactions were weakened as shown by SLS[58-60] and SANS[29] models that were correlated with a reduction in viscosity.[26, 28, 61] In contrast, another mAb, GmAb2, with little charge anisotropy according to the sequence,[9, 13] forms low viscosity solutions[9, 26, 29, 61] and has an S(q) reflective of purely repulsive interactions between mAbs.[55] Consequently, the viscosity of GmAb2 is essentially independent of ionic strength.[26, 29, 61] However, the viscosity increased with salt concentration for a highly hydrophobic mAb, GmAb3.[16, 47, 62] With added salt, GmAb3 dimerized at low concentration, and at high concentration formed larger clusters as observed by S(q) from SANS[16] and SLS which correlated with the high viscosity.[47]

Understanding of static measurements can be further improved with the use of coarse-grained models that approximate mAb shape much more closely than simple spheres. Calero-Rubio et al.[8] developed a series of mAb models suitable for molecular simulation that accounted for steric repulsions, homogeneous vdW surface attractions, and Coulombic long-ranged electrostatic interactions. The models were developed with increasing complexity, ranging from a 3-bead model (one bead per Fab and Fc domain) to an atomistic residue-level model. It was found that 6- and 12-bead models approximately capturing mAb shape achieved the optimal balance of accuracy and computational cost for high concentration simulations.[8] These bead models were accurately fit to low-concentration S(q=0) data from SLS for a moderately interacting mAb and used to successfully predict the high concentration S(q=0) of this mAb.[7] Additional 12-bead models coarse-grained from atomistic models have also been used to predict the formation of clusters at high concentration, which were shown to correlate with mAb viscosities.[9-10, 12] Corbett et. al. found that isotropic (1-bead) models accounting for steric repulsions and homogeneous vdW attractions could quantitatively describe low-q behaviors in S(q), but 3-bead models were required to qualitatively match S(q) profiles up to higher wave vectors.[52] Meanwhile, a very recent study by Wang et al. used 12-bead models to successfully fit mAb S(q)s from SANS across a series of concentrations by including homogeneous short-ranged surface attractions and additional specific bead charges based on mAb sequence. Also, the effects of cluster distributions on mAb diffusion and viscosity were determined.[63] A novel concept, that to our knowledge has not received much attention, if any, is to use S(q) profiles in SAXS or SANS to guide the placement of local anisotropic short-ranged attractions on specific beads to better understand PPI.

Herein, we directly compare SAXS experimental data for a series of mAb solutions up to 250 mg/ml with structural data calculated via liquid-state theory and coarse-grained molecular dynamics simulations to quantify and analyze the underlying PPI. By tuning the attractive PPI via the addition of

NaCl, Arg(HCl), or $ZnSO_4$, we demonstrate systematically a wide range of behavior in structure factors. We also identify upturns at low q for either mAb2 (more weakly interacting and less viscous) with strongly binding $ZnSO_4$ or mAb4 (more strongly interacting and more viscous). A much larger increase in S(q) with the concentration of NaCl shown for mAb4 versus mAb2 indicates the formation of clusters that are shown to increase the viscosity markedly. In the simplest model, the measured effective structure factor $S_{eff}(q)$, which is related to the center of mass S(q) by eq. 1 below[16] is compared with results for optimized isotropic hard-sphere plus attractive Yukawa potentials. Then, to better account for mAb shape, coarse-grained 12-bead models are fit to SAXS form factor measurements at low concentration.[16] The fit 12 bead models are then used in molecular dynamics (MD) simulations at high concentration to directly calculate scattering profiles. To introduce varying degrees of PPI anisotropy (Fab-Fab vs Fab-Fc and Fab-Fab interactions), short-ranged local anisotropic attractions are assigned between select (or all) beads in the Fab and Fc regions via Yukawa potentials. Since the various charge-charge, charge-dipole, dipole-dipole, hydrogen bonding and hydrophobic interactions between molecules may not be fully described *a priori* from the charge obtained from the sequence, it would be desirable to find alternative approaches to describe the PPI. Therefore, we propose a complimentary approach to determine the location and strength of short-ranged local anisotropic attractions by fitting SAXS data with the MD simulations. By comparing simulations to the SAXS $S_{eff}(q)$, we demonstrate that the $S_{eff}(q)$ for solutions of weakly attractive mAb formulations can be fit with uniform potentials on every bead (similar to vdW attraction). However, for more attractive mAbs, it is necessary to add bead-specific attraction in particular locations. Thus, this approach has sufficient sensitivity to discriminate between various models with specific interactions on certain beads based on fits of the experimental $S_{eff}(q)$. These fit models are used to determine a physical picture of the intermolecular structure with real space properties, including radial distribution functions, cluster size distributions (CSD), and nearest neighbor contacts. We show that for a given net attraction the cluster sizes are larger when the attraction has greater angular anisotropy. The CSDs from models that approximate the experimental $S_{eff}(q)$ are then used to model the viscosity behavior in an inverse approach to Kastelic et al. who determined CSDs from viscosities.[49] Ultimately, this class of coarse-grained model and workflow—which is not dependent on prior knowledge of mAb sequence—represents a potentially powerful way of estimating the location and strength of attractive mAb interactions, cluster formation, and viscosity at high concentration.

Materials and Methods

The mAbs used in this study (mAb2 and mAb4) are class Immunoglobulin G (IgG). Both mAbs were provided in respective proprietary buffers with mAb2 being provided at 25 mg/ml and mAb4 (Pfizer) at 3.2 mg/ml. Acetic acid, arginine hydrochloride, histidine, histidine hydrochloride monohydrate, sodium acetate, zinc sulfate, and sodium chloride were purchased from Fisher Scientific, Fairlawn, NJ. And used without further purification. Amicon Ultra-15 Ultracel – 30K centrifugal filters were purchased from Merck Millipore Ltd. Ireland. In this study whenever a protein solution is reported to contain Arg it actually contains Arg and HCl at a 1:1 molar ratio, and any co-solute at an unspecified concentration is 250 mM.

Formation of concentrated mAb solutions

The mAb4 solutions were prepared by centrifugal diafiltration into 30 mM His(HCl) buffer at pH 6 with 250 mM co-solute, followed by centrifugal ultrafiltration as described in previous work,[27] The mAb2 samples were prepared identically, except that the diafiltration buffer was 30 mM (Na)Ace at pH 5.5 without any additional co-solutes. After ultrafiltration 2.5 M solutions of co-solute were mixed with 500 mM (Na)Ace at pH 5.5 and DI water to achieve a solution that was added directly to small aliquots of the mAb2 solutions to achieve the target final co-solute concentration (typically 250 mM) while maintaining 30 mM Na(Ace) buffer and simultaneously achieving the target mAb concentration. Additional details can be found in Section 1 of the ESI.

Viscosity Measurements

The mAb2 sample viscosities were measured using both a microfluidic Viscometer/Rheometer-on-Chip (m-VROC, Rheosense Inc. San Ramon, CA) with a C05 chip and with a syringe viscometer (both at 25°C) described in previous work,[27, 38, 43] and as can be seen in Fig. S14.1.1 the two methods agree within error. The mAb4 sample viscosities were measured at the Rheosense facility in San Ramon, CA on a Rheosense VROC Initium with a B05 chip, which is an automated version of a Rheosense m-VROC. Additional details can be found in Section 14.1 of the ESI.

Small Angle X-ray Scattering (SAXS)

Small angle X-ray scattering (SAXS) was used to measure the structure and infer information about the PPI of select solutions of both mAbs. SAXS measurements were done for mAb2 samples on Bruker Nanostar U SAXS instrument (Bruker AXS, Fitchburg, WI) in high resolution setup equipped with Cu rotating anode source, Vantec 2000 area detector, and scatterless pinholes. Additional measurements were done on a custom SAXSLab setup (SAXSLab, Northampton, MA) equipped with

two scatterless square slits for collimation, Cu rotating anode as a source and PILATUS 300 area detector. The nominal sample to detector distance varied from 1.05 to 1.45m, respectively. The actual sample to detector distance was calibrated using Silver Behenate. The image redaction to 1D data has been done on the corresponding instrumental software. Samples with concentration >5 mg/ml were measured in sealed 1 mm thin-wall quartz capillaries purchased from Charles Supper (Natick, MA). To insure constant scattering volume for improved background subtraction, the dilute samples (5 mg/ml) and corresponding buffers were measured in liquid cells accessories for Nanostar U or SAXSLab instruments that consist of reusable and re-sealable thin-wall capillary tubes. Typical exposure times vary from 1000 to 44000 s depending on a sample concentration. The transmitted and incident x-ray beam intensities were measured either with aid of standardized glassy carbon (for Nanostar U) or with exposure of the detector to a direct beam (for SAXSLab). The >5 mg/ml samples measured on the custom SAXSLab setup were each measured over three *q* ranges. The *I(q)* showed good overlap between ranges (Fig. S1.1) and were combined via weighted averages of the overlap regions. The angle dependent coherent scattering intensity, *I(q)*, of a suspension of asymmetric particles (e.g., mAbs) is represented by

$$I(q) = \phi V_{monomer}(\Delta\rho)^2 P(q)\{1 + \beta(q)[S(q) - 1]\} = \phi V_{monomer}(\Delta\rho)^2 P(q) S_{eff}(q) \quad (1)$$

where $q = \frac{4\pi}{\lambda}\sin\left(\frac{\theta}{2}\right)$, λ is the radiation (x-ray) wavelength and θ is the scattering angle. ϕ is the particle volume fraction, V_{monomer} is the volume of an individual particle, Δρ is the difference between particle and solvent scattering length density, P(q) is the normalized form factor which is the Fourier transformation of intra-particle electron density correlations, S(q) is the structure factor which is related to the Fourier transformation of the inter-particle center of mass distribution, and β(q) is the decoupling function used to decouple intra and inter-particle scattering. The term in braces is often referred to as the effective structure factor, $S_{eff}(q)$, and is equivalent to the concentration normalized I(q) at high concentration, divided by the concentration normalized I(q) at low concentration. When β(q) is ~1, as is the case for low q measurements,[16, 53] the effect of scattering from intra and inter-particle interference can be easily decoupled and $S(q) \approx S_{eff}(q)$.[16, 64] Under dilute conditions inter-particle scattering becomes negligible such that S(q)≈1. Therefore, values of P(q) were measured using dilute (5 mg/ml)[65] mAb solutions. The $S_{eff}(q)$ profiles at high concentration were determined by normalizing the high concentration I(q) with the low concentration P(q). Due to the difficulty in accurately measuring mAb concentration, particularly at high concentration, all SAXS data after solvent correction were scaled by a Porod Law Scaling as previously described.[55]

Fitting scattering data for concentrated mAb solutions via isotropic potential models

Similar to previous work,[16] approximate fits to high concentration $S_{eff}(q)$ profiles were calculated assuming mAbs interact via isotropic hard-sphere Yukawa (HSY) interactions, where Yukawa interactions are attractive. The HSY interparticle potential is given by:

$$\beta u_{HSY}\left(\frac{r}{d_{HSY}}\right) = \begin{cases} \infty & , r/d_{HSY} < 1 \\ -\beta K \frac{e^{-Z\left(\frac{r}{d_{HSY}}-1\right)}}{\frac{r}{d_{HSY}}}, & r/d_{HSY} \geq 1 \end{cases} \quad (2)$$

where $\beta = (k_B T)^{-1}$ (k_B is Boltzmann's constant and T is temperature); r/d_{HSY} is the dimensionless center-to-center interparticle distance; d_{HSY} is the characteristic particle diameter; βK is the dimensionless attraction strength; and Z is the dimensionless inverse characteristic length scale of attractions (analogous to an inverse Debye length). Across the various solutions, the hard-core diameter is $d_{HSY} \approx 90$Å. Structure factors for the HSY potentials were calculated using the Ornstein-Zernike equation and a thermodynamically self-consistent closure relation developed in prior work[66] and previously applied to mAbs.[16]

Simulations of concentrated solutions of 12-bead model mAbs

The mAb shape is approximated by fitting the 5 mg/ml P(q) measurements with a 12-bead model optimization as utilized previously for small SANS measurements of mAbs by Godfrin et al.[16] This approach gives the bead diameter, d_B, and the relative bead positions (the fit bead structures were also used to calculate $\beta(q)$[16]). Concentrated solutions of these 12-bead model mAbs are then simulated via three-dimensional (3D) molecular dynamics (MD) simulations of N_{box}=6000 protein molecules in the NVT ensemble with periodic boundary conditions using LAMMPS.[67] Simulations are initialized with all model mAbs at random positions and orientations within the box with no overlaps. Beads *i* and *j* of two different mAbs interact via the following continuous pair potential, which linearly combines a steeply-repulsive Weeks-Chandler-Andersen (WCA) potential[68] (to model sterics) with, for relevant pairs of beads, a short-ranged attractive well:

$$\beta u_{ij}\left(\frac{r_{ij}}{d_B}\right) = \begin{cases} \beta u_{WCA}\left(\frac{r_{ij}}{d_B}\right) + \beta u_{att}\left(\frac{r_{ij}}{d_B}\right), & r_{ij}/d_B \leq 2^{\frac{1}{24}} \\ \beta u_{att}\left(\frac{r_{ij}}{d_B}\right), & 2^{\frac{1}{24}} < r_{ij}/d_B \leq r_{cut}/d_B \end{cases} \quad (3)$$

where

$$\beta u_{WCA}\left(\frac{r_{ij}}{d_B}\right) = 4\beta\varepsilon_{WCA}\left[\left(\frac{d_B}{r_{ij}}\right)^{48} - \left(\frac{d_B}{r_{ij}}\right)^{24}\right] + \beta\varepsilon_{WCA} \quad (4)$$

and

$$\beta u_{att}\left(\frac{r_{ij}}{d_B}\right) = -\beta K_{ij}\lambda(K_{ij}, Z)\frac{e^{-Z\left(\frac{r_{ij}}{d_B}-1\right)}}{\frac{r_{ij}}{d_B}} \quad (5)$$

Here, r_{ij}/d_B is the dimensionless inter-bead distance, and d_B is the characteristic bead diameter (equivalent to $d_B \approx 35$Å, via the model fitting described above). The characteristic WCA energy scale is set via $\beta\varepsilon_{WCA} = 1$. All intermolecular pairs of beads interact via the steric WCA potential, which accordingly sets the shape of the model mAbs. Attractive contributions are selectively applied between *i*,*j* pairs of beads by setting attraction strengths $\beta K_{i,j}$ to finite values with $\beta K_{i,j} = 0$ if either bead *i* or *j* is not attractive, and $\beta K_{i,j} = K$ if both bead *i* and *j* are attractive. Table 1 shows the various configurations of attractive beads we consider. The value of the dimensionless factor $\lambda(K_{ij}, Z)$ is chosen such that the minimum of the potential function is $\min[\beta u_{ij}] = -\beta K_{ij}$. The (inverse) characteristic length scale of all bead-bead attractions in the main text is $Z = 10$, which corresponds to real-space center to center ranges of approximately $1.1d_B$ (surface to surface separation of ~0.35 nm, which is approximately equal to short-range attraction estimates for mAbs[8, 49, 55, 63, 69]) for all values $\beta K_{i,j}$ considered; thus, a cut-off distance $r_{cut}=2d_B$ for attractive interactions is applied for all systems. All intramolecular interactions between beads are ignored.

We treat the model mAbs as rigid objects and propagate simulation trajectories using an integration time-step of $\Delta t=0.001\ [d_B{}^2 m/(k_B T)]^{1/2}$ (taking the mass of each bead m=1), and fix temperature via a Nose-Hoover thermostat with time-constant $\tau=1000\Delta t$. We set the volumes V_{box} of our cubic simulation boxes based on desired packing fractions $\phi = N_{box}V_{monomer} / V_{box}$, where $V_{monomer}$ is the volume of the 12-bead model mAb (accounting for any slight overlaps between beads). Values for model mAb volume are $V_{monomer} \approx 6.1$ to $6.2\ d_B{}^3$, which given the typical optimized bead size conversion $d_B \approx 35$Å means that $V_{monomer} \approx 260$ nm^3 in real units. Assuming a typical molecular weight of 150 kDa for a mAb (plus, nominally, a hydration layer), we can approximately convert between simulation packing fractions ϕ and experimental densities ρ_e via the convenient relation ρ_e (mg/ml) = (1000 mg/ml)ϕ.

Table 1. Various Rigid 12-Bead Model mAbs Used in MD Simulations for Comparison with Experimental SAXS Data.

12-bead model	domain-domain attractions	generality of attraction	no. attractive beads per monomer	diagram
Steric only	N/A	N/A	0	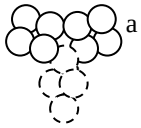 a
All4	Fab-Fab Fab-Fc Fc-Fc	4 beads per domain	12	 a
All1	Fab-Fab Fab-Fc Fc-Fc	1 specific bead per domain	3	 a
FabFab1	Fab-Fab	1 specific bead per domain	2	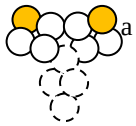 a

a. Unfilled beads are subject to only excluded volume interactions (purely-repulsive WCA potentials) with unfilled beads of another model mAb, while gold beads are additionally subject to mutual attractions (WCA potentials combined with attractive Yukawa potentials). Beads corresponding to the Fab and Fc regions have solid and dashed outlines, respectively, and are drawn to scale.

Structure factors for concentrated solutions of 12-bead model mAbs

To make direct comparisons with experimental $S_{eff}(q)$, we first calculate reciprocal-space intensity profiles $I(q)$ for the 12-bead model simulations for the various configurations and strengths of attractive beads at monomer packing fractions ϕ commensurate with experimental suspension densities. To obtain $I(q)$, we first extract the coordinates of all model mAb beads in an instantaneous configuration and distribute n_S points randomly within the volume of each bead. Positions are generated relative to bead

centers such that $n_S \gg 1$ points would result in a uniform point-density; this is equivalent to all mAb regions having uniform scattering length density. We calculate the real-space pair-correlations $\rho(r)$ between these points (analogous to a radial distribution function $g(r)$) and then obtain the non-normalized scattering intensity $I(q)$ via numerical Fourier Transform inversion of $\rho(r)$. Practically, we choose $n_s = 10$ so that there are $7.2\text{x}10^5$ points distributed per configuration, where we correspondingly find that $\rho(r)$ profiles (and $I(q)$ profiles) converge given 400-500 input configurations. Analogous to experiments, we then obtain effective structure factors via the relation $S_{\text{eff}}(q) \sim I(q)\ \phi_0 / [P(q)\ \phi]$, where $\phi_0 = 0.005$ as the form factor the model P(q) is fit to experimental data at 5 mg/ml (see discussion above). We then renormalize the reciprocal space axis from units of ${d_B}^{-1}$ to Å^{-1} via the fitted bead size $d_B \approx 35\text{Å}$.

Aggregate morphologies of 12-bead model mAbs at finite concentration

To characterize multibody morphology as a function of configuration and strength of attractive beads, we calculate (1) cluster size distributions (CSDs) that quantify the instantaneous probability $p(n)$ of observing aggregates comprising $n \leq n_{\text{box}}$ model monomers; and (2) probability distributions $p(n_{\text{neigh}})$ of the number of direct (nominally, nearest) neighbors to the monomers. Here, two monomers are considered direct neighbors if any two of their beads (one from each monomer) are within $r_{\text{neigh}}=1.1d_B$ of one another, where this cutoff distance is the approximate range of attractive wells for all finite βK values considered given our choice of $Z = 10d_B^{-1}$. We consider all possible bead pairs between two monomers, rather than only mutually attractive beads, as this allows us to analyze all systems—including those with no attractions—on a common basis. Analogous to previous studies,[12, 70] we consider two monomers part of the same aggregate if they are direct neighbors and/or if they are connected by a continuous path (i.e., set) of clustered monomers.

Second osmotic virial coefficients of 12-bead model mAbs

The second osmotic virial coefficient B_{22} is approximated for each of the configurations of mutually attractive beads and attraction strengths via the expression

$$B_{22} = -\frac{1}{2}\int_V \left[e^{-\beta U(\vec{r})} - 1\right] d\vec{\boldsymbol{r}} \approx -\frac{V}{2n_t}\sum_i^{n_t}\left[e^{-\beta U(\vec{\boldsymbol{r}}_i)} - 1\right] \quad (6)$$

where $U(\vec{\boldsymbol{r}}_i)$ is the *total* interaction energy between two 12-bead model mAbs in trial i of n_t trials. Over all trials, the first 12-bead model is fixed in space, while $\vec{\boldsymbol{r}}_i$ is the relative center of mass (COM) distance and orientation of the second model mAb, with position and orientation randomly generated. V is the volume available for placement of the second mAb; here, this volume chosen is a sphere, with the largest allowable COM distance (radius of the sphere) chosen for a particular configuration of attraction beads

such that all possible realizations of the second mAb at that (and larger) distances result in no interactions. B_{22} values were calculated in attraction strength increments of $\Delta\beta K$=0.05 or 0.10, depending on the local rate of change in B_{22} with respect to βK. For convergence of B_{22} within a tolerance of $10^{-4}\ {d_B}^3$, the number of trials ranged from n_t=10^7 for the weakest attractions to 10^8 for the strongest βK values considered. For the steric-only case where no beads exhibit attractions, we find $B_{22,St} = 57.4\ {d_B}^3$, which corresponds to an effective excluded volume of approximately $B_{22,St} = 2460$ nm^3. This is comparable with previous work by Calero-Rubio et al. that found $B_{22,St} = 2390$ nm^3 for an atomistic model of a different mAb.[8]

Results and Discussion

Deriving 12-bead model mAb from experimental form factor P(q)

In order to use SAXS to infer PPI at high concentration from $S_{eff}(q)$ it is first necessary to assign a mAb shape from P(q) measured at low concentration.[16, 53, 64-65, 71] P(q) was measured for 5 mg/ml solutions of mAb2 at various ionic strengths with 0, 50, and 250 mM NaCl, as well as with 250 mM Arg. P(q) for mAb4 solutions at 5 mg/ml with either 250 mM NaCl or Arg were also measured. The radii of gyration, R_g, and maximum dimensions, D_{max}, were calculated by Guinier analysis of each P(q) measurement (shown in Table S2.1), and the resulting values all fall within the expected range of mAb monomer sizes (R_g~5 nm, D_{max}<15 nm). Thus, none of these solutions exhibit significant mAb dimerization at low concentration.[16, 47, 62] The measured P(q) were then fit using a previously published algorithm[16] that approximates the average mAb shape in solution as a collection of 12 spherical beads. Several previous studies have determined that 12-bead models represent mAb shape with a meaningful level of detail,[7-10, 12, 16, 63] even compared to atomistic models.[7-8] The fit P(q) is in excellent agreement with the data (Fig. S2.1). The best fit bead diameter and Fab-Fab and Fab-Fc domain separations are shown in Table S2.2 and are found to be very similar to the structure in the 12-bead model from Calero-Rubio et al.[8] Fig. S2.2 can be used as a guide to demonstrate the indicated domain separations. The similarity in structure suggests that mAb2 and mAb4 have the same general size and shape, and that co-solutes only weakly affect their average conformations. The location of the center of each bead in each fit mAb structure is listed in Table S2.3. The high concentration 12-bead model simulations below were run with the bead structure fit to the mAb2: Arg solution P(q), but were also tested for the structure fit to the mAb4: NaCl solution P(q) in some cases. As seen in Fig. S6.1, the different bead structures did not qualitatively effect the simulations.

Effects of protein concentration and co-solute on experimental structure factor profiles

The effect of ionic strength on the $S_{eff}(q)$ of mAb2 solutions is shown in Fig. 1 for 0, 50, and 250 mM NaCl as well as 250 mM Arg. $S_{eff}(q)$ of mAb2 solutions for 300-500 mM NaCl is shown in Fig. S4.2. At high q (q>~0.04 A^{-1}) where $S_{eff}(q)$ is mostly affected by mAb shape and flexibility,[53] all solutions have similar $S_{eff}(q)$ behavior. The $S_{eff}(q)$ values approach 1 at q>0.1 A^{-1} and have a small shoulder at q≈0.06 A^{-1} (~10 nm lengthscale as estimated by Bragg length $l_{Bragg} = \frac{2\pi}{q}$, typical of mAb hydrodynamic diameter[16, 72-73]), which has been seen for many other mAbs.[16, 50-52, 55, 63] The effect of adding co-solutes is most pronounced at lower q values, where the profile is more strongly dependent on underlying PPI.[16, 55, 63] For mAb2 (Fig. 1A), $S_{eff}(q)$ is the smallest (most repulsive) for the no co-solute control. As NaCl is added $S_{eff}(q)$ at low q increases indicating more attractive PPI and at 250 mM NaCl, the curvature of $S_{eff}(q)$ changes, with a slight upturn at q < 0.03 A^{-1}. Further addition of NaCl has little impact on $S_{eff}(q)$, and beyond 350 mM it decreases (Fig. S4.2). Here, note that the 50 mM NaCl solution in Fig. 1A is at a higher protein concentration (144 mg/ml) than the other solutions, which reduces its $S_{eff}(q)$.[55] However, according to previous S(0) data from SLS, which all agree within error of the S(0) from SAXS of these same solutions as shown in Fig. S3.1, the 50 mM NaCl curve is still expected to have a low q $S_{eff}(q)$ in between those of 250 mM Arg and NaCl. The addition of Arg also increases $S_{eff}(q)$ relative to the no co-solute control, but much less than for NaCl at the same ionic strength. In many cases, Arg has been found to weaken short range attractions.[74-78] Even for the less attractive mAb2, we found that the addition of strong bridging interactions with 35 mM divalent Zn^{2+} in $ZnSO_4$ would produce an upturn in S(q) at low q (Fig. S4.1A).

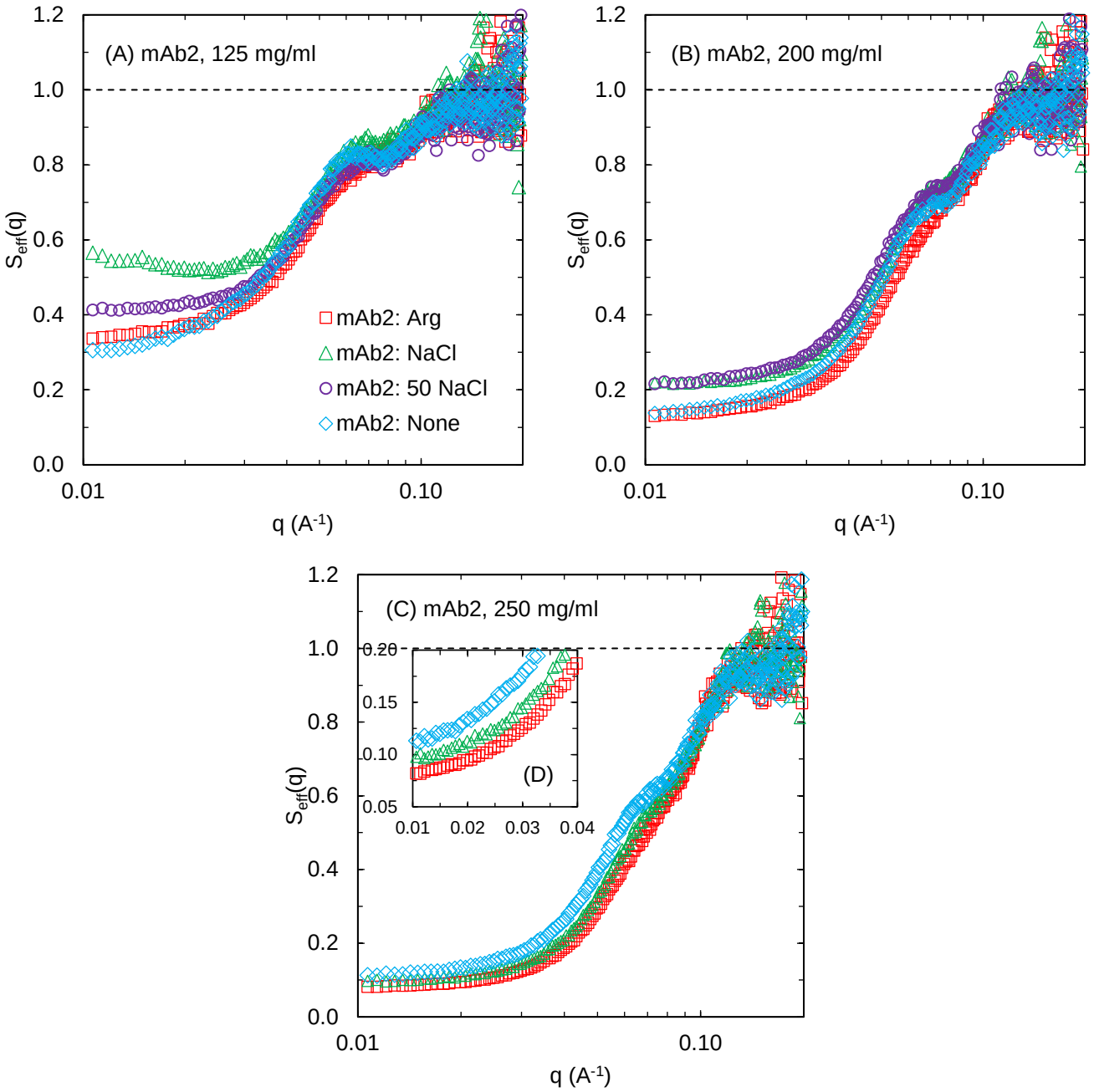

Figure 1. Structure factors $S_{eff}(q)$ measured via SAXS for solutions of mAb2 at (A) 125 mg/ml, (B) 200 mg/ml, and (C) 250 mg/ml with no additional co-solutes (blue diamonds), 250 mM Arg (red squares), 50 mM NaCl (purple circles), and 250 mM NaCl (green triangles). Panel (D) inset shows zoom of low-q limits of $S_{eff}(q)$ for data at 250 mg/ml. The 50 mM NaCl sample is not shown in Panel (C), because the highest measured concentration for this solution was 225 mg/ml, not 250 mg/ml. The value of S(0) for this solution can be found in Fig. S3.1.

The difference in the effects of added co-solute on $S_{eff}(q)$ decrease with increasing mAb concentration, as seen at 200 and 250 mg/ml in Fig. 1B and C, respectively. $S_{eff}(q)$ at low q decreases

with mAb concentration for all samples. However, the differences between samples become smaller as steric repulsion plays a greater role relative to attraction. The greater steric constraints at the higher concentration hinder the alignment of attractive sites into energetically favorable orientations, and consequently, the net attraction becomes more similar for the various systems.[55] Additionally, the relative order of attraction changes with higher ionic strength solutions becoming relatively less attractive with concentration though the differences between all samples at high concentration are small.

Hard Sphere Yukawa Model of the SAXS Data

Fig. 2 shows $S_{eff}(q)$ for both mAb2 and mAb4 at 125 mg/ml under high ionic strength conditions (250 mM NaCl or Arg), where the long-ranged electrostatic interactions should be minor (highly screened).[8, 63] The behavior at high q (>0.04 A^{-1}) is similar for the two mAbs, but at low q $S_{eff}(q)$ for mAb4 (particularly with NaCl) is curved upward indicating strong attraction. The differences in S(0) and slopes in $S_{eff}(q)$ at low q are summarized in Table S5.1. Each of these $S_{eff}(q)$ curves was fit with a HSY potential (eq. 2) (lines in Fig. 2, along with a pure hard sphere potential) with d = 9 nm (volume fraction of 0.19 at 125 mg/ml), approximately the measured diameter of gyration (Table S2.1). This d is similar to previous values that approximate mAbs as spheres.[16, 53, 55] The best fit K and Z for the HSY potentials of each solution are summarized in Table S5.1. The best fit mAb2 solutions had Z=13, indicating a ~0.7 nm characteristic length scale, as expected for local anisotropic short-ranged attraction. In contrast, much longer attraction length scales of Z=3 to 4, (~2 to 3 nm) were observed for mAb4 solutions. These long attraction length scales cannot be explained by electrostatic interactions as the Debye length of these solutions is ~0.6 nm; however, they are required to achieve the upward curvature at low q with isotropic models.[55, 63] As demonstrated below, these extreme parameterizations are not required for more physically-plausible estimates of PPI from coarse-grained mAb models that capture monomer shape and anisotropic PPI. (Further discussion is also given in Section 5 of the ESI.)

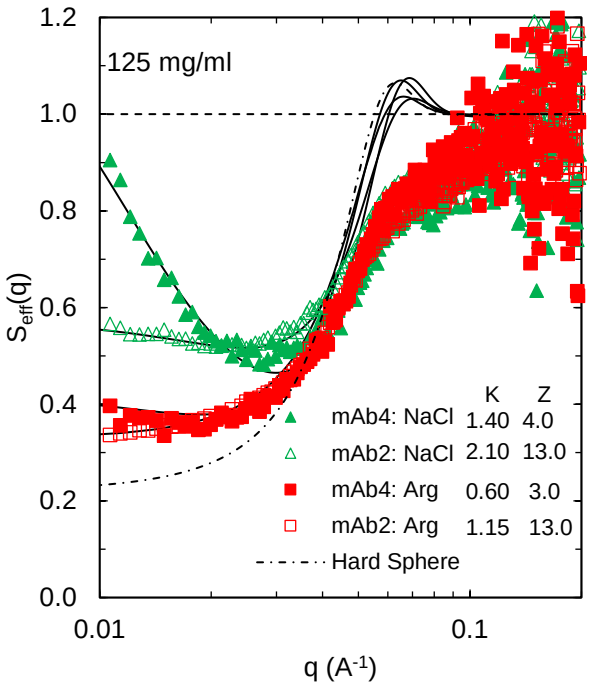

Figure 2. Structure factors $S_{eff}(q)$ measured via SAXS for solutions of mAb2 and mAb4 at 125 mg/ml with 250 mM of listed co-solutes (symbols same as Fig. 1). Black lines show structure factors calculated via integral equation theory based on isotropic interactions between (single-bead) monomers. Solid lines correspond to short-range attractive HSY potentials, with well-depths K and inverse characteristic lengthscales Z given in the legend. Dashed line corresponds to a hard-sphere potential. All fits assume a hard-sphere diameter corresponding to 9 nm.

Molecular Dynamics Simulations of Concentrated 12-bead Model mAbs

To gain further insight into the effect of attractive interactions on particular mAb sites, $S_{eff}(q)$ profiles at high concentrations, which are compared with experimental data, were calculated via MD simulations of the 12-bead mAb models determined from low concentration P(q) measurements. The 12-bead structure allows for the incorporation of anisotropic attractions approximating possible Fab-Fab, Fab-Fc, etc. interactions in a logical and strategic manner (Table 1). These models are used to discriminate among $S_{eff}(q)$ behavior resulting from anisotropic (All1 and FabFab1) versus "uniform" attractions (All4), as well as among different types of relevant classes of anisotropic attractions (Fab-Fab, Fab-Fc, and Fc-Fc).[9, 12, 28] Across the various models, PPIs were implemented via attractive Yukawa potentials with short ranges (Z=10, corresponding characteristic lengthscale of 0.35 nm) that were added to select beads to test the three models displayed in Table 1, while all of the 12-beads had the same steric repulsion (eq. 3).

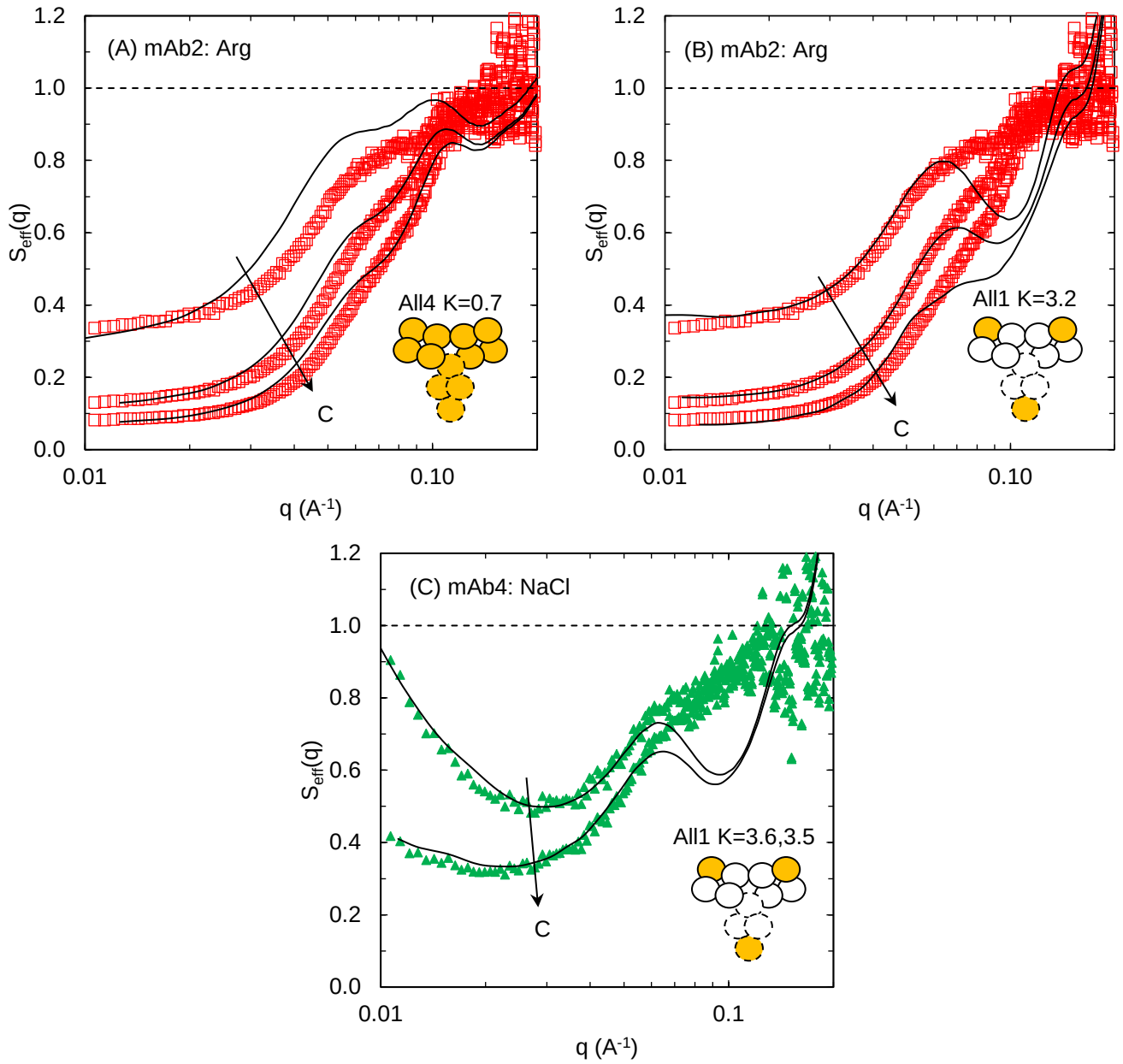

Figure 3. Structure factors $S_{eff}(q)$ measured via SAXS for mAb data and simulated profiles for 12-bead models that best-matched data across all concentrations. (A) mAb2: Arg at 125, 200 and 250 mg/ml fit with All4 K=0.7; (B) mAb2: Arg at 125, 200 and 250 mg/ml fit with All1 K=3.2; and (C) mAb4: NaCl at 125 and 165 mg/ml fit with All1 K=3.6 at 125 mg/ml and All1 K=3.5 at 165 mg/ml.

These 12-bead models are able to closely fit the long-range ($q < 0.06$ A^{-1}) structure for both the highly attractive (mAb4: NaCl) and weakly attractive (mAb2: Arg) systems across the mAb concentrations tested (Fig. 3) given appropriate choices of attractive configurations and strengths. To quantify goodness of fit, the root mean square deviation (RMSD) for the region of interest ($q < 0.06$ A^{-1})

was calculated as shown in Table 3 for best fit systems. Given the small shoulder consistently seen at $q \approx 0.06$ A^{-1} at the lengthscale of the mAb monomer (~10 nm), . the chosen q range represents interparticle correlations that characterize PPI. As shown in Fig. 3, the mAb2: Arg systems can be fit at low q across the mAb concentrations tested with a constant attraction strength parameter (All4 K=0.7 and All1 K=3.2). In the case of mAb4: NaCl, the attraction of the best fit model at 125 mg/ml (All1 K=3.6) has to be slightly reduced to fit at 165 mg/ml (K=3.5). Fig. S12.1 also shows that mAb2: Arg and mAb4: Arg can be fit across concentrations by FabFab1 K=3.5 and All1 K=3.2, respectively. All of these fits were achieved with a constant, physically relevant attraction length scale of 0.35 nm (from Z=10), whereas it was necessary to vary Z in the HSY spherical model. For mAbs, a weakly changing interaction potential across concentrations has been successful previously for fits of S(q) from SANS,[63] or S(0) from SLS.[7] At high-q the bead models can only qualitatively fit the mAb data (as seen previously),[52, 63] as shown in Figs. 2-3. These high q fits could likely be improved by adding molecular flexibility,[53, 63] which will be examined systematically in future work.

Given the different numbers and configurations of attractive beads in the various models, it is useful to compare their net attractions. As shown in Fig. 4, we calculated (1) normalized second osmotic virial coefficients $B_{22}/B_{22,St}$ (where $B_{22,St} = B_{22}$ in the steric-only case with K=0), and (2) approximate whole-model attraction strengths K_{tot}. Here, we define K_{tot} as simply the well-depth K multiplied by the number of attractive beads per mAb as shown in Table 1 (this does not explicitly account for inaccessible portions of the attractive wells). As expected, the models with more attractive beads exhibit lower (more net attractive) $B_{22}/B_{22,St}$ values for the same K (Fig. 4A). When compared against K_{tot} (Fig. 4B), all models have similar $B_{22}/B_{22,St}$ when $K_{tot} < 6.5$, but deviate at higher K_{tot}. For a given K_{tot}, $B_{22}/B_{22,St}$ is more attractive for the All1 and FabFab1 models with attraction spread over fewer beads, since the exposed attractive beads have a larger "influence" than the less exposed interior beads. The best fit models (Fig. 3) had $B_{22}/B_{22,St}$ values within the range of 0.25 to 1.0, so simulations were run with K values that yielded $B_{22}/B_{22,St}$ of approximately 0.75, 0.50 and 0.25 (summarized in Table 2), along with select additional values used to fit specific experimental profiles. As shown for both measured (Fig. 1) and simulated (Figs. S12.2 and S12.3) $S_{eff}(q)$, the variation in $S_{eff}(q)$ between samples is greater at 125 mg/ml than at higher concentrations (due to steric constraints), so the following discussion will focus on the results at 125 mg/ml before considering higher concentrations.

Table 2. Summary of Structural Properties Extracted from MD Simulations of the Various 12-Bead Models (at C=125 mg/ml) Corresponding to $B_{22}/B_{22,St}$ = 0.75, 0.50 and 0.25.

Model	K (k_BT)	K_{tot} (k_BT)	$B_{22}/B_{22,St}$	S(0)	Slope (A) S(q<0.015 A^{-1})	$\langle n \rangle$	$\langle n_{neigh} \rangle$
Steric	0.0	0.0	1.00	0.19	4.7	1.1	0.1
All4	0.7	8.4	0.75	0.31	6.1	1.4	0.3
All4	1.0	12.0	0.53	0.62	4.3	2.5	0.7
All4	1.2	14.4	0.28	2.2	-87	16	1.5
All1	2.7	8.1	0.74	0.24	3.9	1.9	0.56
All1	3.5	10.5	0.49	0.70	-20	1100	1.8
All1	3.9	11.7	0.27	2.4	-330	5200	3.7
FabFab1	3.7	7.4	0.76	0.40	7.9	4.3	1.1
FabFab1	4.5	9.0	0.50	1.1	35	4800	3.9
FabFab1	4.9	9.8	0.26	1.2	40	5800	4.4

All4 Model. In Fig. 5 for the All4 model, with identical attraction on every bead, the K was altered from 0.7 to 1 k_BT to test the sensitivity of $S_{eff}(q)$. (Additional K values are shown in Fig. S9.1). As can be seen in Fig. 5A an increase in K from 0 (steric only) to 1 k_BT caused a steady increase in S(0) with little effect on $S_{eff}(q)$ curvature at low q. The K=0.7 simulation closely resembled the mAb2: Arg data (at low q), but none of the simulations fit the other mAb solutions that will be shown to have stronger and more anisotropic attraction. This potential with K=0.7 is very similar to that used for uniform vdW potentials in previous studies, which all show vdW attraction magnitudes of ~0.7 k_BT, as discussed in Section 7 of the ESI.[7, 63] Since this model closely fits mAb2: Arg, anisotropic attractions are likely very weak in that system. Values of S(0) and slopes of $S_{eff}(q)$ at low q for select simulations are tabulated in Table 2 (while those of all simulations tested are in Table S13.1 and S13.2, respectively).

In addition to $S_{eff}(q)$, it is useful to extract real-space structural properties from the simulations to further characterize the mAb self-association. The center of mass (COM) radial distribution function, $g_{COM}(r)$, (Fig. 5B) of the steric only simulation (K=0) reaches a maximum at ~3.5d_B, which is equivalent to slightly more than 1 full diameter of gyration, d_g, of the 12-bead structure. Note that this is the $g_{COM}(r)$ between two 12-bead structures, not individual beads. The limited probability of finding two steric only mAbs at distances smaller than d_g suggests that there is little inter-digitation and minimal overlap of the three arms without the presence of attraction. The $g_{COM}(r)$ then has very slight periodic

oscillations at larger separation distances, but essentially reaches bulk behavior ($g_{COM}(r)=1$) by $6d_B$ ($<2d_g$). The lack of long-range structure in the K=0 model correlates with minimal self-association as seen in the cumulative cluster size distribution (CSD) in Fig. 5C, where *n* is the aggregation state of the protein (*n*=1 is monomer, 2 is dimer, etc) and *C(n)* is the cumulative probability of a protein being in state *n*. Fig. 5C shows that with K=0, >93% of the mAbs are monomeric, and >99% are either monomer or dimers (because of the finite probability that two mAbs may instantaneously collide). To complement these data, the differential or non-cumulative CSD ($p(n)$) is shown in Fig. S9.1E.

The real space properties can also be used to understand how the solution structure is affected by attraction. Increasing K from 0 to 1.2 causes the formation of small oligomers with the average cluster sizes, $\langle n \rangle$, increasing from ~1.1 to ~2.5 (Fig. 5C and Table 2, all samples in Table S13.3). The $g_{COM}(r)$ plots demonstrate that these oligomers have tightly packed COMs as the peak at ~d_g becomes more diffuse and the periodic oscillations at $r>d_g$ are further reduced. The reduction in long range structure is shown more clearly in the transformed $g_{COM}(r)$ shown in Fig. S9.1F.[79] The inset in the bottom right of Fig. 5B (and Fig. S8.1A) indicates the COM separation ($r\sim2.8d_B$) of two mAbs with Fab regions directly on top of each other. Therefore, most orientations with multiple ($\geq$4) beads interacting simultaneously will have $r<2.8d_B$. Since all the beads are attractive, these multi-interacting bead orientations are enthalpically favorable for this model, explaining why increasing K only increases $g_{COM}(r)$ in this separation range. In fact, when the attraction is strong enough, sharp peaks appear at separations of d_B and in some cases (K>1) at $2d_B$. These peaks are almost certainly aphysical and occur from stacking of the rigid 12-bead configurations (see upper left and middle insets and Fig. S8.1E), which allows for all 12-beads to simultaneously reside in the attractive well of neighboring beads. The average number of nearest neighbors, $\langle n_{neigh} \rangle$, for these simulations is tabulated in Table 2 (and for all simulations in Table S13.4). The tight packing of these simulated mAbs helps limit network formation as even at K=1 almost none of the mAbs have more than 2 nearest neighbor contacts, as seen in Fig. 5D. This result reflects that the oligomers are almost all tightly packed structures without branching points, minimizing the possibility of system spanning networks.[12]

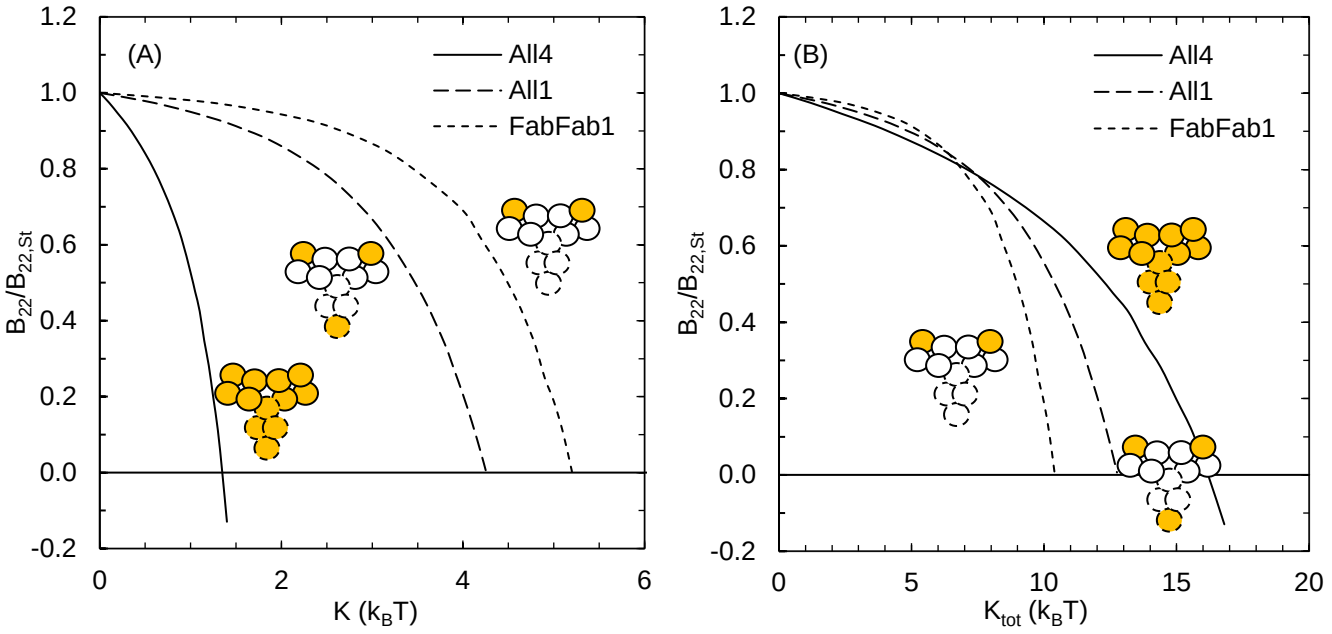

Figure 4. (A) Osmotic second virial coefficient ratio $B_{22}/B_{22,St}$ (where $B_{22,St}$ = 2460 nm^3 is the steric-only coefficient) for the various 12-bead models versus attraction strength K applied at corresponding beads. (B) Ratio $B_{22}/B_{22,St}$ for the various models versus total approximate attraction strength K_{tot} over the same ranges in K as in (A).

All1 Model. Since upward curvature at low-q could not be achieved with a uniform (All4) potential, the All1 model was tested. It includes all interaction types (Fab-Fab, Fab-Fc and Fc-Fc) but only 1 attractive bead at the "tip" of each domain (see Table 1) (Fig. 6A). Here, the increase in S(0) with K for All1 is accompanied by a significant increase in upward curvature in $S_{eff}(q)$ at low q. This curvature captures the low q (long range) structure for the mAb4: NaCl system, and nearly fits that of mAb4: Arg, unlike All4. However, the All1 model does not qualitatively fit the data at high q as it has a peak in $S_{eff}(q)$ at q~0.06 A^{-1} and a trough at ~0.1 A^{-1} indicating more ordered structure at short-range than seen in the SAXS data. The ability to more accurately fit these data will likely require the inclusion of mAb flexibility[53, 63] and/or a non-zero attraction on the other 9 beads near the center of mass. Both of these alterations will facilitate a higher degree of configuration space for mAbs to sample in the ensemble of possible states.

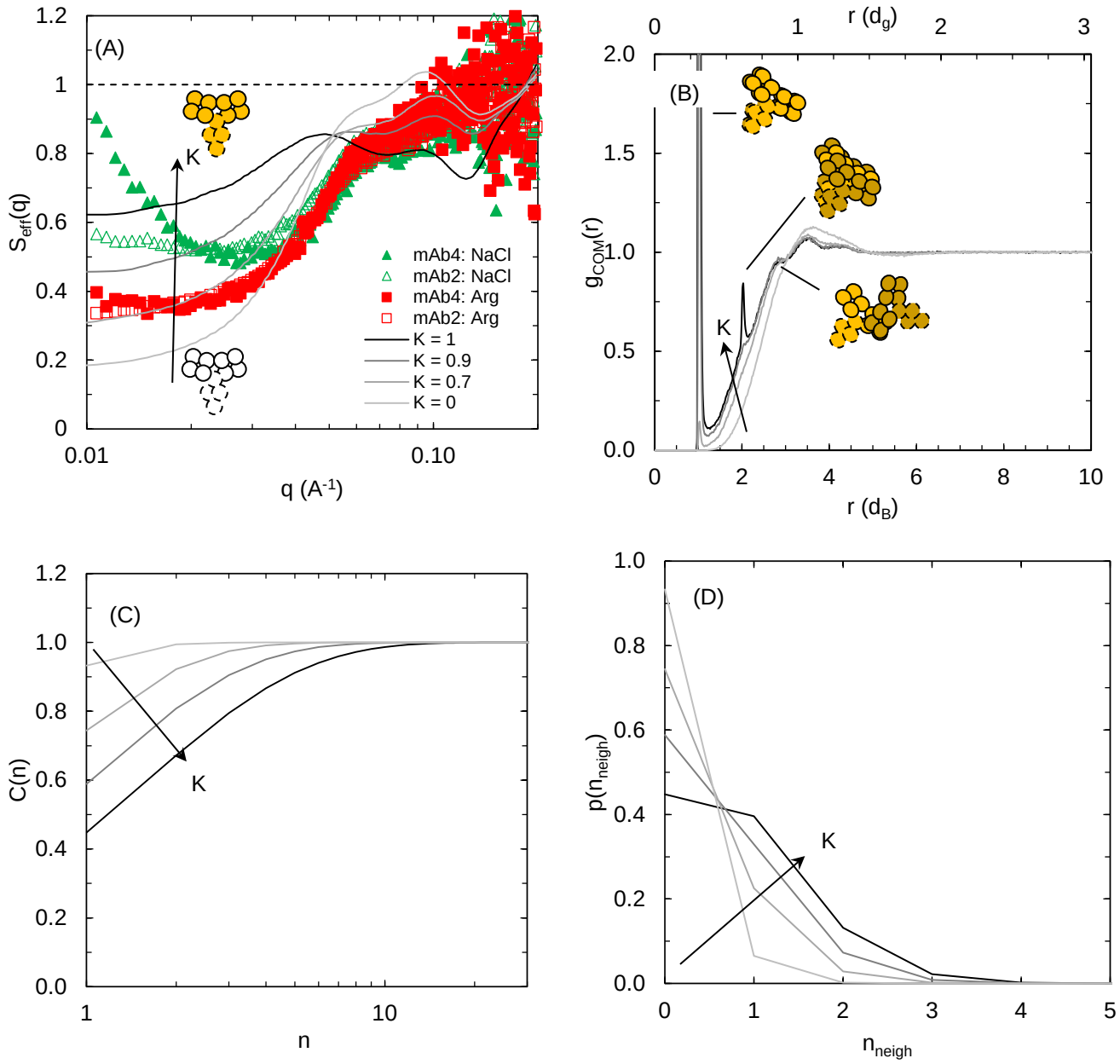

Figure 5. (A) Structure factors $S_{eff}(q)$ of select mAb solutions at 125 mg/ml (symbols) compared with profiles from All4 model simulations given various K (lines). (B) Corresponding radial distribution functions $g_{COM}(r)$ based on 12-bead model center of mass; (C) corresponding cumulative CSD profiles; and (D) probability distributions of the number of nearest neighbors. In panel (B), diagrams illustrate neighbor configurations corresponding to $g_{COM}(r)$ peaks at high K-values, and first peak maxima for K=0.9 and K=1.0 at $r=d_B$ are g(r)=4.8 and 19.6, respectively.

The more realistic $S_{eff}(q)$ curvature in the All1 model versus All4 at high attraction corresponds with very different solution structure in real space. An increase in K for the All1 model increases the $g_{COM}(r)$ at $r<d_g$ but without the "aphysical" narrow peaks in the All4 model. The longest achievable

COM separation with attractive beads in contact is represented by the inset in Fig. 6B (and Fig. S8.1F). This distance r=4.6d_B corresponds with the end of the first peak in $g_{COM}(r)$, suggesting that this peak represents the first coordination shell. Additionally, increasing K causes increased periodicity at r>d_g with deeper troughs and higher peaks at long distances signifying the formation of a more long-ranged structure (also seen in transformed $g_{COM}(r)$ in Fig. S8.2F). The long range structure can also be seen in the cumulative CSD in Fig. 6C as higher K causes association of much larger species, eventually, producing percolating networks that span the simulation box when K>3.4. These networks correspond directly with the upturn in $S_{eff}(q)$ at low q. Fig. 6D shows the distribution of nearest neighbors. Despite only having three attractive beads, many of the simulations show that more than three neighbors are present. At high values of K, multiple mAbs simultaneously interact with the same attractive bead, as is illustrated with a possible geometric arrangement in Fig. S8.2. Thus, this model (and likely other 12-bead models)[7-10, 12, 63] produce behavior that is not considered in theoretical models that limit the binding to one protein per attractive site.[48-49] Here the K is spread on the surface area of the entire bead, and the large attractive area allows for high coordination numbers that would not be observed for attractive patches that are smaller than the bead surface area.

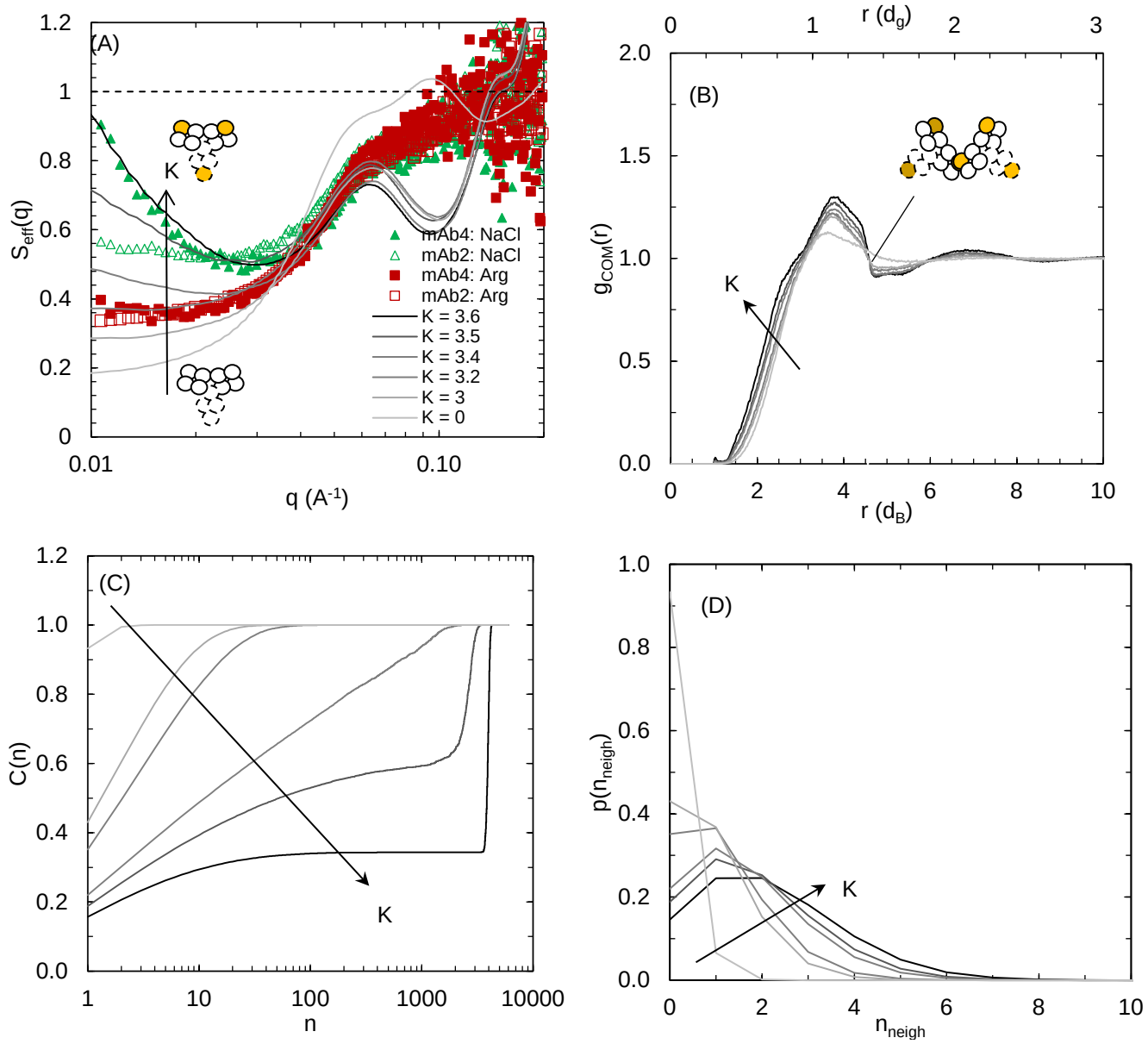

Figure 6. (A) Structure factors $S_{eff}(q)$ of select mAb solutions at 125 mg/ml (symbols) compared with profiles from All1 model simulations given various K (lines). (B) Corresponding radial distribution functions $g_{COM}(r)$ based on 12-bead model center of mass; (C) corresponding cumulative CSD profiles; and (D) probability distributions of the number of nearest neighbors. In panel (B), diagram illustrates the neighbor configuration corresponding to the outer boundary of the broad first-maximum in $g_{COM}(r)$.

FabFab1 Model. The FabFab1 model, which has only 1 attractive bead per Fab domain and thus only Fab-Fab attractions (see Table 1) is shown in Fig. S9.3. At low K (K=3.5) this model produces an $S_{eff}(q)$ that closely matches mAb2: Arg behavior at low q. However, the FabFab1 model strongly deviates from the data for the more attractive systems with higher K as a prominent intermediate range

order (IRO) peak in $S_{eff}(q)$ develops at q~0.02 A^{-1}. This IRO peak corresponds with a most prevalent cluster size of *n*~10 shown as a peak in p(*n*) in Fig. S9.3E. The IRO and most prevalent cluster sizes form due to steric hindrance from the 10 non-attractive beads resisting binding from additional mAbs and is discussed in Section 10 of the ESI. Despite this resistance, increasing K for FabFab1 increases the long range structure seen in $g_{COM}(r)$ and increases the self-association in the CSDs markedly, even forming percolating networks at K $\geq$4.5. Therefore, the formation of a preferred cluster size and a percolating network can occur simultaneously in this model, that is a cluster percolated systems.[80] As in the All1 model, this model can have more than two nearest neighbors as multiple mAbs can simultaneously be attracted to the same bead in 3D space (i.e., weak valence limitation). Because this model has an IRO peak in $S_{eff}(q)$ and is therefore qualitatively different than any published mAb data we restrict further discussion of this model to the ESI.

Comparison of 12-Bead Model Simulations for Best Fits of Experimental $S_{eff}(q)$

The attention is now focused on only the best fits of the experimental $S_{eff}(q)$ data. As shown in Fig. 7A, any model with weak attraction ($B_{22}/B_{22,St}$~0.75) can reasonably fit at low q the simple downward sloping mAb2: None and mAb4: None controls, as well as mAb2: Arg data with RMSD values in Table 3. As seen in Table 3 (RMSDs), and Fig. 7A, the All1 model is a better fit to the data for 0.02 $A^{-1} \leq q \leq$ 0.06 A^{-1}, whereas the All4 model is more attractive than the data in that q range but is better able to capture the curvature at q < 0.02 A^{-1}. The All1 model best fits mAb4: Arg since it captures the upturn at low q. For mAb2, the curvature of $S_{eff}(q)$ at low q increases with increasing NaCl concentration up to 250 mM (Fig. S4.2) suggesting a transition from uniform attraction (similar to the All4 model) to anisotropic attraction (similar to the All1 model). At NaCl concentrations greater than 350 mM the upturn remains, but $S_{eff}(q)$ at low q decreases indicating weaker overall short-ranged attraction. Only the All1 model can reasonably fit the more attractive mAb4: NaCl.

The effect of adding co-solutes is significantly different for the two mAbs indicating distinct classes of mAb PPI behavior. The $S_{eff}(q)$ of mAb4: None is slightly more repulsive than that of mAb2: None. Interestingly, it becomes much more attractive for mAb4 with the pronounced upturn at low q with 250 mM NaCl.

Figs. 7B – D show that the best fit systems to mAb2: None and mAb4: None have relatively little long-range structure (by $g_{COM}(r)$), only small clusters ($1.4 < \langle n \rangle < 6.4$) and few nearest neighbors, consistent with weak attraction. Since the same simulations that best describe mAb2: None also approximate mAb2: Arg, the addition of arginine does not significantly affect the size of clusters

formed. For mAb4, the effect of adding Arg is more pronounced, as the best fit simulation forms larger clusters and the $g_{COM}(r)$ shows greater long-range oscillations relative to the no co-solute control. The best fit model to mAb4: NaCl has much greater long-ranged structure in $g_{COM}(r)$, much more self-association (forming percolating networks), and greater nearest neighbor contacts. In contrast, clusters are not present for mAb4: None. This self-association behavior in response to added salt is similar to mAbs previously reported in literature, such as GmAb3[15-16, 57], suggesting that they belong to the same class.

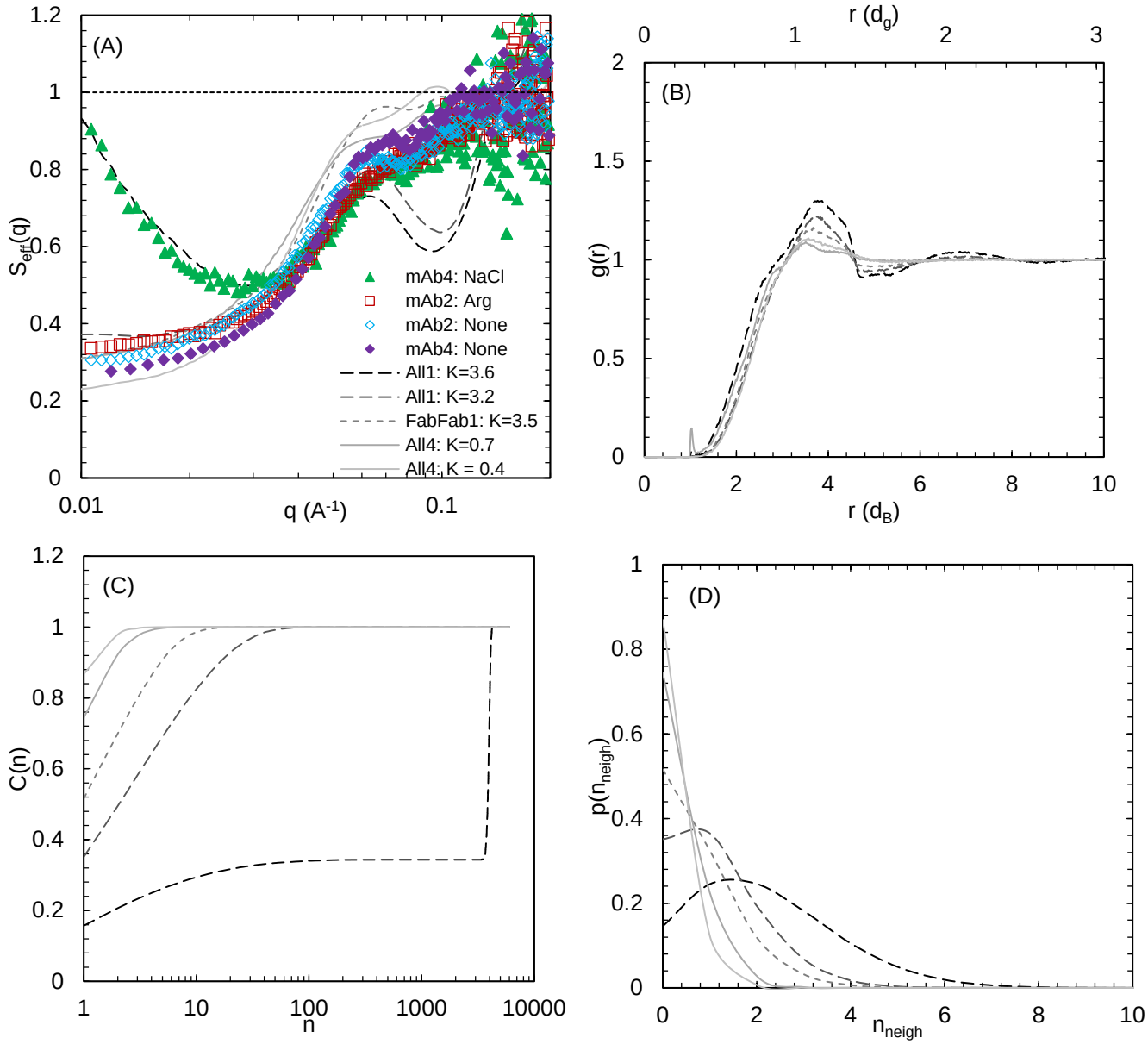

Figure 7. (A) Structure factors $S_{eff}(q)$ of select mAb solutions at 125 mg/ml (symbols) compared with profiles from 12-bead model simulations that best-fit experimental data (lines). (B) Corresponding radial distribution functions $g_{COM}(r)$ based on

12-bead model center of mass; (C) corresponding cumulative CSD profiles; and (D) probability distributions of the number of nearest neighbors.

Given that the best fit parameters in Fig. 7 have already been shown in Fig. 3 and S12.1 to give comparable fits of $S_{eff}(q)$ at higher mAb concentration, it is instructive to examine the behavior of real space properties. As shown in Fig. S12.6, increasing mAb concentration consistently raises $g_{COM}(r)$ at $r<d_g$, but only weakly increases periodicity beyond the first coordination shell (see also Fig. S12.9). It also causes large increases in self-association and nearest neighbors for the All1 and FabFab1 models as shown in Fig. S12.7 and S12.8, respectively, while only modestly increasing association for the All4 (and steric only models Fig. S12.5). Increasing the mAb concentration makes the $S_{eff}(q)$ of all systems (data and simulations) appear more repulsive (S(0) decreases and the magnitude of the $S_{eff}(q)$ slope is reduced), while simultaneously increasing self-association. The key properties of these simulations at 125 and 200 mg/ml are summarized in Table 3, which shows that the three models that fit mAb2: Arg have vastly different $\langle n \rangle$ (2.3 for All4 K=0.7, 23 for FabFab1 K=3.5 and 3900 for All1 K=3.2). As discussed below, the simplest All4 model will be shown to be the most relevant on the basis of the relatively low solution viscosity for this system.

Table 3. Summary of Structural Properties Extracted from MD Simulations for 12-Bead Models that Best Fit the Structure Factors from Experiments.

Experiments			**12-bead model simulations**							
System[a]	**Conc. (mg/ml)**	**η_r**	**Best Fit Model(s)**	**RMSD for q<0.06 A^{-1}**	**K_{tot}**	**$B_{22}/B_{22,St}$**	**S(0)**	**Slope (A) S(q<0.015 A^{-1})**	**$\langle n \rangle$**	**$\langle n_{neigh} \rangle$**
mAb2: Arg	125	6.1	All4 K=0.7	0.101	8.4	0.75	0.31	6.1	1.4	0.3
			FabFab1 K=3.5	0.090	7	0.79	0.31	6.7	2.4	0.7
			All1 K=3.2	0.022	9.6	0.60	0.37	-1.3	6.4	1.1
	200	27	All4 K=0.7	0.051	8.4	0.75	0.13	2.9	2.3	0.64
			FabFab1 K=3.5	0.038	7	0.79	0.13	5.0	23	1.6
			All1 K=3.2	0.013	9.6	0.60	0.14	0.86	3910	2.2
	250	94	All4 K=0.7	0.040	8.4	0.75	0.08	1.9	4.1	0.92
			FabFab1 K=3.5	0.049	7	0.79	0.08	3.3	2510	2.2
			All1 K=3.2	0.022	9.6	0.60	0.07	0.40	5460	3.2
mAb4: Arg	125	8.4	All1 K=3.2	0.025	9.6	0.60	0.37	-1.3	6.4	1.1
	165	23	All1 K=3.2	0.029	9.6	0.60	0.21	0.83	1530	1.7
mAb4: NaCl	125	21	All1 K=3.6	0.023	10.8	0.44	0.90	-48	2600	2.1
	165	92	All1 K=3.5	0.017	10.5	0.49	0.41	-9.4	4640	2.6

a. Note that mAb2: NaCl is not included as no 12-bead models closely fit its $S_{eff}(q)$.

Comparison of the Models at Constant $B_{22}/B_{22,St}$

Comparison of the three models (All4, All1, FabFab1) at 125 mg/ml and constant $B_{22}/B_{22,St}$ shows that systems with more anisotropic attraction (FabFab1>All1>All4) have more self-association $\langle n \rangle$, and nearest neighbors, $\langle n_{neigh} \rangle$, relative to those with more uniform attraction (seen in Table 2 and Figs. S11.2 and S11.3). These results demonstrate how measurements of net PPI (such as B_{22} or k_D) that do not account for anisotropy may have limited predictive power for high concentration viscosity and aggregation. As suggested previously,[18, 45] high concentration PPI can be dominated by a few particularly attractive orientations, which are not extensively sampled by low-concentration measurements thereby limiting their predictive power of solution behavior at high concentration.[81] Furthermore, by considering the analogy between their structures, the behavior of our 12-bead models is consistent with patchy spherical colloids, which have been shown to have a higher likelihood to crystallize (analogous to self-association) with smaller attractive patches compared to those with larger weak patches.[82] We hypothesize that this behavior is caused by the entropic cost of having large areas of surface contacts. For example, at a given net attraction ($B_{22}/B_{22,St}$ or K_{tot}) the K value of All1 is 3 to 4 times stronger than that of All4. Therefore, the All4 model requires 3 to 4 simultaneously interacting beads to match the enthalpic gain as All1 with a single interacting bead. Since there are far fewer orientations involving 3 to 4 bead contacts, All4 has a significantly higher entropic penalty than All1 for the same enthalpic benefit. This causes self-association to be generally less favorable for All4 than All1. Additionally, having multiple attractive beads causes the self-association for All4 to be more compact than All1, as shown by $g_{COM}(r)$.

Comparison to Previous 12-Bead Models

Previous 12-bead simulations of concentrated mAb solutions[7-10, 12, 63] modeled mAb interactions through steric repulsion, uniform vdW attraction, and Coulombic electrostatic interactions with bead charges determined by the sequence. These models were successful in predicting high concentration S(0) from low concentration measurements[7], and in fitting S(q) over a range of mAb concentrations and salinities.[63] However, at ionic strengths similar to the present work (~270 mM) the long ranged electrostatic contributions in these models become negligible (Fig. S7.2). The comparisons of mAb4: NaCl and mAb2: Arg clearly demonstrate that the short-ranged anisotropic interactions can be extremely important. Since these interactions have varying length scales,[69] and depend in a complex manner on the specific topology of the protein surface,[81] it is reasonable to model them with a short-ranged attractive

Yukawa potential with a single attraction strength K.[16, 53] Currently, these attractions are added without knowledge of the mAb sequence, but future studies could use these simulations to determine amino acid motifs that reflect these short-range attractions, to ultimately enable prediction from mAb sequence. Additionally, future studies may add long ranged Coulombic electrostatic potentials (in addition to short ranged anisotropic attraction) and hinge flexibility to more accurately capture a wider range of solution conditions and solution/mAb structure, respectively.

mAb Solution Viscosities and Role of Cluster Size Distribution

The relative viscosities of the Arg and NaCl mAb solutions (both mAb2 and mAb4) were measured versus mAb concentration. The cluster size from SAXS and viscosity increased in the same order mAb2: Arg < mAb4: Arg < mAb4: NaCl (Fig. S14.2.1). To examine this relationship, the viscosities were first analyzed with the Ross-Minton and entanglement models (section 14.2 and 14.3 of the ESI). The Ross-Minton equation showed some indication of cluster formation at high concentration for all systems, but most strongly for mAb4: NaCl (in accordance with SAXS). Similarly, the fit attraction strengths from the entanglement model correlated directly with the attraction strengths determined from SAXS (Fig. S14.3.2) and was strongest for mAb4: NaCl and weakest for mAb2: Arg.

To more quantitatively address the influence of cluster size on viscosity, we have extended an empirical viscosity relation recently developed by Kastelic et al.[49] The relation is given by:

$$\ln\left(\frac{\eta}{\eta_0}\right) = \sum_{n=1}^{\infty} c f(n) p(n,c) \quad (7)$$

$$f(n) = bn^d \quad (8)$$

where c is the mass concentration, $p(n,c)$ is the normalized weight fraction distribution of clusters of size *n* (n-mer) in solution (identical to CSD), and b and d are adjustable parameters, with *d* indicating how strongly clusters influence viscosity. As d increases, larger clusters cause greater increases in viscosity.[49] The $p(n,c)$ was already determined directly from best fit simulations to the SAXS data (Fig. 7C and S12.7) and *b* and *d* were fit to the viscosity data. Because multiple models (All1 K=0.7, FabFab1 K=3.5, and All1 K=3.2) yielded good fits to mAb2: Arg each of these models was fit separately along with All1 K=3.5 and 3.6 to mAb4: NaCl (K=3.6 was used for 125 mg/ml and K=3.5 for 165 mg/ml data). It was assumed the simulations that fit mAb2: Arg SAXS data at 125, 200 and 250 mg/ml, would also describe the behavior at 165 mg/ml. When needed, the experimental viscosities were interpolated from the measurements using the Ross-Minton equation (eq. S14.2.1). Fig. 8 shows the model in Eq. 7 provides good fits of the viscosity vs concentration profiles for mAb2: Arg and mAb4: NaCl with universal values of b and d, and $p(n,c)$ determined from simulations of SAXS $S_{eff}(q)$ data. In contrast,

other models that fit the mAb2: Arg SAXS data well (All1 K=3.2 and FabFab1 K=3.5) were far less accurate for the viscosity as shown in Fig. S14.4.1 and Table S14.4.1, as an excess degree of anisotropy (cluster formation) over-predicted the degree of clustering. Therefore, this viscosity model appears to be useful for discriminating among candidate coarse-grained models, to further complement fits of $S_{eff}(q)$.

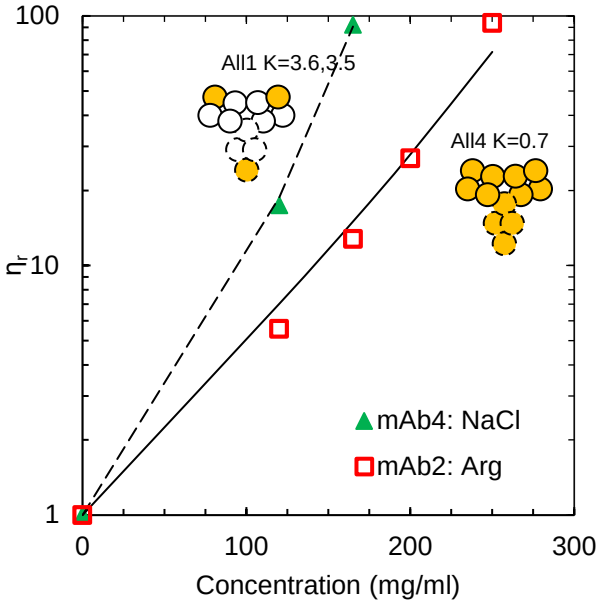

Figure 8. Measured relative viscosity versus mAb concentration (symbols) for mAb4: NaCl and mAb2: Arg with corresponding fits to eq. 7 (lines). The $p(n,c)$ distribution inputs to eq. 7 were determined from 12-bead model simulations. For mAb2: Arg, the All4 K=0.7 model was used at all concentrations. For mAb4: NaCl, the All1 K=3.6 and All1 K=3.5 models were used for 125 and 165 mg/ml, respectively. The parameters *b* and *d* were fit to be 16.0 ml/g and 0.0687, respectively.

Conclusions

From $S_{eff}(q)$ versus q measured with a benchtop SAXS instrument, various classes of behavior may be observed in PPI for concentrated mAb solutions for various co-solute conditions. As the NaCl increases S_{eff} (q) increases much more rapidly for mAb4 and with a much larger upturn at low q compared to mAb2 indicating more strongly attractive class of behavior. Modeling of the $S_{eff}(q)$ of concentrated protein solutions with coarse-grained 12-bead MD simulations provides new insight into short ranged anisotropic attraction, and real space properties including the cluster size distribution (CSD) and $g_{COM}(r)$. At high ionic strength where long ranged Coulombic interactions are nearly negligible, the van der Waals and short ranged anisotropic attractive interactions are described successfully with a single Yukawa attraction parameter K on specified beads, and a fixed screening length, Z^{-1}=0.35 nm. For systems such as mab2: Arg with weak attraction, $S_{eff}(q)$ is small at low q and

may be modeled with a uniform potential on all beads resulting in minimal self-association. For a strongly attractive system, mAb4: NaCl, only the All1 model with an attractive site in each Fab and the Fc regions (Fab-Fab, Fab-Fc, and Fc-Fc interactions) can fit the upturn in $S_{eff}(q)$ at low q. This upturn is shown to be related to long-ranged order in the form of percolated networks according to the CSD ($\langle n \rangle \sim 2590$) and $g_{COM}(r)$. The $S_{eff}(q)$ profiles could be fit over mAb concentrations from 125 to 250 mg/ml with a constant K value. More fundamentally, in agreement with previous studies,[81-82] the models show that for similar net attraction ($B_{22}/B_{22,St}$), models with stronger specific attractions (FabFab1>All1>All4) form larger clusters and have more nearest neighbors than those with more uniform attractions.

In our new approach, the selectivity among bead interactions comes from insertion of a Yukawa attraction on strategic beads on the basis of fits to SAXS $S_{eff}(q)$ data with simulations at high concentration. In previous 12-bead models[7-9, 12, 63] the selectivity was produced from charges given by the mAb sequence. Ultimately, it would be of interest to combine the two approaches. The ability to discriminate between models with bead interactions at particular Fab and Fc bead sites from SAXS simulations, and to provide real space properties (CSD and $g_{COM}(r)$), will be of interest in engineering protein sequence and formulating protein solutions for weak PPI to minimize aggregation and viscosities. The viscosity may be calculated more accurately given the CSD[49], which can be obtained directly from the simulations of the SAXS $S_{eff}(q)$. These advances may be expected to play an important role in mAb discovery, processing, storage and administration given the small sample volume needs for SAXS at high concentration, the ease of experimental measurement, and the advancement in development of coarse-grained bead model simulations.

Supporting Information

Detailed information on sample preparation; the low concentration SAXS form factor measurements and fits; comparison of S(0) from SAXS and SLS measurements; $S_{eff}(q)$ measurements for both mAbs in additional co-solute systems; fits to $S_{eff}(q)$ at concentrations above 125 mg/ml with the HSY potential; comparison of the effects of 12-bead shape on MD simulations; comparisons of the interaction potentials used in the current study with previous studies; real space visualization of the MD simulations; results of MD simulations with additional K values, along with p(n) and the transformed g(r); discussion of the FabFab1 model; comparisons between different bead models at equivalent values of B_{22}; the effect of mAb concentration on MD simulations; summary tables of all MD simulations;

experimental details for viscosity measurements as well as additional modelling of viscosity with the Ross-Minton, entanglement and Kastelic models are supplied as Supporting Information.

Acknowledgements

The authors gratefully acknowledge Merck & Company, Inc., Pfizer Inc. and the Welch Foundation (F-1696 and F-1319) for their financial support. This research used resources of the Center for Functional Nanomaterials, which is a U.S. DOE Office of Science Facility, at Brookhaven National Laboratory under Contract No. DE-SC0012704. The authors also acknowledge NSF-MRI award 1624659 for funding the custom SAXSLab instrument used in this research.

References

1. Reichert, J. M. Therapeutic monoclonal antibodies approved or in review in the European Union or United States. https://www.antibodysociety.org/resources/approved-antibodies/ (accessed 6/14/2019).
2. Carter, P. J., Potent antibody therapeutics by design. *Nat. Rev. Immunol.* **2006,** *6* (5), 343-357.
3. Shire, S. J.; Shahrokh, Z.; Liu, J., Challenges in the development of high protein concentration formulations. *J. Pharm. Sci.* **2004,** *93* (6), 1390-1402.
4. Roberts, C. J., Protein Aggregation and Its Impact on Product Quality. *Current Opinion in Biotechnology* **2014,** *30*, 211-217.
5. Wang, W., Advanced protein formulations. *Protein Sci.* **2015,** *24* (7), 1031-1039.
6. Chari, R.; Jerath, K.; Badkar, A. V.; Kalonia, D. S., Long- and short-range electrostatic interactions affect the rheology of highly concentrated antibody solutions. *Pharm. Res.* **2009,** *26* (12), 2607-18.
7. Calero-Rubio, C.; Ghosh, R.; Saluja, A.; Roberts, C. J., Predicting protein-protein interactions of concentrated antibody solutions using dilute solution data and coarse-grained molecular models. *J. Pharm. Sci.* **2017**.
8. Calero-Rubio, C.; Saluja, A.; Roberts, C. J., Coarse-Grained Antibody Models for "Weak" Protein-Protein Interactions from Low to High Concentrations. *J. Phys. Chem. B* **2016,** *120* (27), 6592-605.
9. Chaudhri, A.; Zarraga, I. E.; Kamerzell, T. J.; Brandt, J. P.; Patapoff, T. W.; Shire, S. J.; Voth, G. A., Coarse-Grained Modeling of the Self-Association of Therapeutic Monoclonal Antibodies. *J. Phys. Chem. B* **2012,** *116* (28), 8045-57.
10. Chaudhri, A.; Zarraga, I. E.; Yadav, S.; Patapoff, T. W.; Shire, S. J.; Voth, G. A., The Role of Amino Acid Sequence in the Self-Association of Therapeutic Monoclonal Antibodies: Insights from Coarse-Grained Modeling. *J. Phys. Chem. B* **2013,** *117* (5), 1269-79.
11. Woldeyes, M. A.; Calero-Rubio, C.; Furst, E. M.; Roberts, C. J., Predicting Protein Interactions of Concentrated Globular Protein Solutions Using Colloidal Models. *J. Phys. Chem. B* **2017,** *121* (18), 4756-4767.
12. Buck, P. M.; Chaudhri, A.; Kumar, S.; Singh, S. K., Highly viscous antibody solutions are a consequence of network formation caused by domain-domain electrostatic complementarities: insights from coarse-grained simulations. *Mol. Pharm.* **2015,** *12* (1), 127-139.
13. Yadav, S.; Laue, T. M.; Kalonia, D. S.; Singh, S. N.; Shire, S. J., The influence of charge distribution on self-association and viscosity behavior of monoclonal antibody solutions. *Mol. Pharmaceutics* **2012,** *9* (4), 791-802.

14. Roberts, C. J.; Blanco, M. A., Role of Anisotropic Interactions for Proteins and Patchy Nanoparticles. *J. Phys. Chem. B* **2014,** *118* (44), 12599-611.
15. Lilyestrom, W. G.; Yadav, S.; Shire, S. J.; Scherer, T. M., Monoclonal antibody self-association, cluster formation, and rheology at high concentrations. *J. Phys. Chem. B.* **2013,** *117* (21), 6373-6384.
16. Godfrin, P. D.; Zarzar, J.; Zarraga, I. E.; Porcar, L.; Falus, P.; Wagner, N. J.; Liu, Y., Effect of hierarchical cluster formation on the viscosity of concentrated monoclonal antibody formulations studied by neutron scattering. *J. Phys. Chem. B.* **2016**.
17. Ghosh, R.; Calero-Rubio, C.; Saluja, A.; Roberts, C. J., Relating Protein-Protein Interactions and Aggregation Rates From Low to High Concentrations. *J. Pharm. Sci.* **2016,** *105* (3), 1086-96.
18. Connolly, B. D.; Petry, C.; Yadav, S.; Demeule, B.; Ciaccio, N.; Moore, J. M.; Shire, S. J.; Gokarn, Y. R., Weak interactions govern the viscosity of concentrated antibody solutions: high-throughput analysis using the diffusion interaction parameter. *Biophys. J.* **2012,** *103* (1), 69-78.
19. Burckbuchler, V.; Mekhloufi, G.; Paillard Giteau, A.; Grossiord, J. L.; Huille, S.; Agnely, F., Rheological and syringeability properties of highly concentrated human polyclonal immunoglobulin solutions. *Eur. J. Pharm. Biopharm.* **2010,** *76* (3), 351-356.
20. Yadav, S.; Shire, S. J.; Kalonia, D. S., Factors affecting the viscosity in high concentration solutions of different monoclonal antibodies. *J. Pharm. Sci.* **2010,** *99* (12), 4812-4829.
21. Carpenter, J. F.; Randolph, T. W.; Jiskoot, W.; Crommelin, D. J. A.; Middaugh, C. R.; Winter, G.; Fan, Y. X.; Kirshner, S.; Verthelyi, D.; Kozlowski, S.; Clouse, K. A.; Swann, P. G.; Rosenberg, A.; Cherney, B., Overlooking subvisible particles in therapeutic protein products: gaps that may compromise product quality. *J. Pharm. Sci.* **2009,** *98* (4), 1201-1205.
22. Sharma, V. K.; Patapoff, T. W.; Kabakoff, B.; Pai, S.; Hilario, E.; Zhang, B.; Li, C.; Borisov, O.; Kelley, R. F.; Chorny, I.; Zhou, J. Z.; Dill, K. A.; Swartz, T. E., In silico selection of therapeutic antibodies for development: Viscosity, clearance, and chemical stability. *Proc. Natl. Acad. Sci. U. S. A.* **2014,** *111* (52), 18601-18606.
23. Li, L.; Kumar, S.; Buck, P. M.; Burns, C.; Lavoie, J.; Singh, S. K.; Warne, N. W.; Nichols, P.; Luksha, N.; Boardman, D., Concentration dependent viscosity of monoclonal antibody solutions: explaining experimental behavior in terms of molecular properties. *Pharm. Res.* **2014,** *31* (11), 3161-78.
24. Agrawal, N. J.; Helk, B.; Kumar, S.; Mody, N.; Sathish, H. A.; Samra, H. S.; Buck, P. M.; Li, L.; Trout, B. L., Computational tool for the early screening of monoclonal antibodies for their viscosities. *Mabs* **2016,** *8* (1), 43-8.
25. Tomar, D. S.; Li, L.; Broulidakis, M. P.; Luksha, N. G.; Burns, C. T.; Singh, S. K.; Kumar, S., In-silico prediction of concentration-dependent viscosity curves for monoclonal antibody solutions. *Mabs* **2017,** *9* (3), 476-489.
26. Liu, W.; Cellmer, T.; Keerl, D.; Prausnitz, J. M.; Blanch, H. W., Interactions of lysozyme in guanidinium chloride solutions from static and dynamic light-scattering measurements. *Biotechnol. Bioeng.* **2005,** *90* (4), 482-490.
27. Dear, B. J.; Hung, J. J.; Truskett, T. M.; Johnston, K. P., Contrasting the influence of cationic amino acids on the viscosity and stability of a highly concentrated monoclonal antibody. *Pharm Res* **2017,** *34* (1), 193-207.
28. Kanai, S.; Liu, J.; Patapoff, T. W.; Shire, S. J., Reversible self-association of a concentrated monoclonal antibody solution mediated by fab-fab interaction that impacts solution viscosity. *J Pharm Sci* **2008,** *97* (10), 4219-4227.
29. Yearley, E. J.; Godfrin, P. D.; Perevozchikova, T.; Zhang, H.; Falus, P.; Porcar, L.; Nagao, M.; Curtis, J. E.; Gawande, P.; Taing, R.; Zarraga, I. E.; Wagner, N. J.; Liu, Y., Observation of Small

Cluster Formation in Concentrated Monoclonal Antibody Solutions and its Implications to Solution Viscosity. *Biophys. J.* **2014,** *106* (8), 1763-70.
30. Laber, J. R.; Dear, B. J.; Martins, M. L.; Jackson, D. E.; DiVenere, A.; Gollihar, J. D.; Ellington, A. D.; Truskett, T. M.; Johnston, K. P.; Maynard, J. A., Charge Shielding Prevents Aggregation of Supercharged GFP Variants at High Protein Concentration. *Mol. Pharmaceutics* **2017,** *14* (10), 3269-3280.
31. He, F.; Woods, C.; Litowski, J.; Roschen, L.; Gadgil, H.; Razinkov, V.; Kerwin, B., Effect of sugar molecules on the viscosity of high concentration monoclonal antibody solutions. *Pharm. Res.* **2011,** *28* (7), 1552-1560.
32. Borwankar, A. U.; Dinin, A. K.; Laber, J. R.; Twu, A.; Wilson, B. K.; Maynard, J. A.; Truskett, T. M.; Johnston, K. P., Tunable equilibrium nanocluster dispersions at high protein concentrations. *Soft Matter* **2013,** *9* (6), 1766.
33. Johnston, K. P.; Maynard, J. A.; Truskett, T. M.; Borwankar, A.; Miller, M. A.; Wilson, B.; Dinin, A. K.; Khan, T. A.; Kaczorowski, K. J., Concentrated dispersions of equilibrium protein nanoclusters that reversibly dissociate into active monomers. *ACS Nano* **2012**.
34. Du, W.; Klibanov, A. M., Hydrophobic Salts Markedly Diminish Viscosity of Concentrated Protein Solutions. *Biotechnol. Bioeng.* **2011,** *108* (3), 632-6.
35. Guo, Z.; Chen, A.; Nassar, R. A.; Helk, B.; Mueller, C.; Tang, Y.; Gupta, K.; Klibanov, A. M., Structure-activity relationship for hydrophobic salts as viscosity-lowering excipients for concentrated solutions of monoclonal antibodies. *Pharm. Res.* **2012,** *29* (11), 3102-9.
36. Wang, S.; Zhang, N.; Hu, T.; Dai, W.; Feng, X.; Zhang, X.; Qian, F., Viscosity-Lowering Effect of Amino Acids and Salts on Highly Concentrated Solutions of Two IgG1 Monoclonal Antibodies. *Mol. Pharmaceutics* **2015,** *12* (12), 4478-87.
37. Whitaker, N.; Xiong, J.; Pace, S. E.; Kumar, V.; Middaugh, C. R.; Joshi, S. B.; Volkin, D. B., A formulation development approach to identify and select stable ultra-high-concentration monoclonal antibody formulations with reduced viscosities. *J. Pharm. Sci.* **2017,** *106* (11), 3230-3241.
38. Borwankar, A. U.; Dear, B. J.; Twu, A.; Hung, J. J.; Dinin, A. K.; Wilson, B. K.; Yue, J.; Maynard, J. A.; Truskett, T. M.; Johnston, K. P., Viscosity reduction of a concentrated monoclonal antibody with arginine·HCl and arginine·glutamate. *Ind. Eng. Chem. Res.* **2016**.
39. Binabaji, E.; Rao, S.; Zydney, A. L., The Osmotic Pressure of Highly Concentrated Monoclonal Antibody Solutions: Effect of Solution Conditions. *Biotechnol. Bioeng.* **2014,** *111* (3), 529-536.
40. Fukuda, M.; Moriyama, C.; Yamazaki, T.; Imaeda, Y.; Koga, A., Quantitative Correlation between Viscosity of Concentrated MAb Solutions and Particle Size Parameters Obtained from Small-Angle X-ray Scattering. *Pharm. Res.* **2015**.
41. Fukuda, M.; Watanabe, A.; Hayasaka, A.; Muraoka, M.; Hori, Y.; Yamazaki, T.; Imaeda, Y.; Koga, A., Small-scale screening method for low-viscosity antibody solutions using small-angle X-ray scattering. *Eur. J. Pharm. Biopharm.* **2017,** *112*, 132-137.
42. Fukuda, M.; Kameoka, D.; Torizawa, T.; Saitoh, S.; Yasutake, M.; Imaeda, Y.; Koga, A.; Mizutani, A., Thermodynamic and fluorescence analyses to determine mechanisms of IgG1 stabilization and destabilization by arginine. *Pharm. Res.* **2014,** *31* (4), 992-1001.
43. Hung, J. J.; Borwankar, A. U.; Dear, B. J.; Truskett, T. M.; Johnston, K. P., High concentration tangential flow ultrafiltration of stable monoclonal antibody solutions with low viscosities. *J. Membr. Sci.* **2016,** *508*, 113-126.
44. Hung, J. J.; Dear, B. J.; Dinin, A. K.; Borwankar, A. U.; Mehta, S. K.; Truskett, T. T.; Johnston, K. P., Improving viscosity and stability of a highly concentrated monoclonal antibody solution with concentrated proline. *Pharm. Res.* **2018,** *35* (7), 133.

45. Saito, S.; Hasegawa, J.; Kobayashi, N.; Kishi, N.; Uchiyama, S.; Fukui, K., Behavior of Monoclonal Antibodies: Relation Between the Second Virial Coefficient (B (2)) at Low Concentrations and Aggregation Propensity and Viscosity at High Concentrations. *Pharm. Res.* **2012,** *29* (2), 397-410.
46. Ross, P. D.; Minton, A. P., Hard quasi-spherical model for viscosity of hemoglobin solutions. *Biochem. Biophys. Res. Commun.* **1977,** *76* (4), 971-976.
47. Lilyestrom, W. G.; Yadav, S.; Shire, S. J.; Scherer, T. M., Monoclonal Antibody Self-Association, Cluster Formation, and Rheology at High Concentrations. *J. Phys. Chem. B* **2013,** *117* (21), 6373-84.
48. Schmit, J. D.; He, F.; Mishra, S.; Ketchem, R. R.; Woods, C. E.; Kerwin, B. A., Entanglement model of antibody viscosity. *J. Phys. Chem. B* **2014,** *118* (19), 5044-9.
49. Kastelic, M.; Dill, K. A.; Kalyuzhnyi, Y. V.; Vlachy, V., Controlling the viscosities of antibody solutions through control of their binding sites. *J Mol Liq* **2017**.
50. Inouye, H.; Houde, D.; Temel, D. B.; Makowski, L., Utility of Solution X-Ray Scattering for the Development of Antibody Biopharmaceuticals. *J. Pharm. Sci.* **2016,** *105* (11), 3278-3289.
51. Mosbaek, C. R.; Konarev, P. V.; Svergun, D. I.; Rischel, C.; Vestergaard, B., High concentration formulation studies of an IgG2 antibody using small angle x-ray scattering. *Pharm. Res.* **2012,** *29* (8), 2225-2235.
52. Corbett, D.; Hebditch, M.; Keeling, R.; Ke, P.; Ekizoglou, S.; Sarangapani, P.; Pathak, J.; Van Der Walle, C. F.; Uddin, S.; Baldock, C.; Avendano, C.; Curtis, R. A., Coarse-grained modeling of antibodies from small-angle scattering profiles. *J. Phys. Chem. B.* **2017,** *121* (35), 8276-8290.
53. Castellanos, M. M.; Clark, N. J.; Watson, M. C.; Krueger, S.; McAuley, A.; Curtis, J. E., Role of Molecular Flexibility and Colloidal Descriptions of Proteins in Crowded Environments from Small-Angle Scattering. *J. Phys. Chem. B* **2016,** *120* (49), 12511-12518.
54. Castellanos, Maria M.; Pathak, Jai A.; Leach, W.; Bishop, Steven M.; Colby, Ralph H., Explaining the non-Newtonian character of aggregating monoclonal antibody aolutions using small-angle neutron scattering. *Biophys. J.* **2014,** *107* (2), 469-476.
55. Yearley, E. J.; Zarraga, I. E.; Shire, S. J.; Scherer, T. M.; Gokarn, Y.; Wagner, N. J.; Liu, Y., Small-angle neutron scattering characterization of monoclonal antibody conformations and interactions at high concentrations. *Biophys. J.* **2013,** *105* (3), 720-731.
56. Blanco, M. A.; Sahin, E.; Li, Y.; Roberts, C. J., Reexamining protein-protein and protein-solvent interactions from Kirkwood-Buff analysis of light scattering in multi-component solutions. *J Chem Phys* **2011,** *134* (22), 225103.
57. Wang, W.; Lilyestrom, W. G.; Hu, Z. Y.; Scherer, T. M., Cluster size and quinary structure determine the rheological effects of antibody self-association at high concentrations. *J. Phys. Chem. B.* **2018,** *122* (7), 2138-2154.
58. Scherer, T. M.; Liu, J.; Shire, S. J.; Minton, A. I., Intermolecular Interactions of IgG1 Monoclonal Antibodies at High Concentrations Characterized by Light Scattering. *J. Phys. Chem. B* **2010,** *114* (40), 12948-12957.
59. Scherer, T. M., Cosolute Effects on the Chemical Potential and Interactions of an IgG1 Monoclonal Antibody at High Concentrations. *J. Phys. Chem. B* **2013,** *117* (8), 2254-66.
60. Scherer, T. M., The role of cosolute-protein interactions in the dissociation of monoclonal antibody clusters. *J. Phys. Chem. B.* **2015**.
61. Zarraga, I. E.; Taing, R.; Zarzar, J.; Luoma, J.; Hsiung, J.; Patel, A.; Lim, F. J., High Shear Rheology and Anisotropy in Concentrated Solutions of Monoclonal Antibodies. *J. Pharm. Sci.* **2013,** *102* (8), 2538-49.

62. Wang, W.; Lilyestrom, W. G.; Hu, Z. Y.; Scherer, T. M., Cluster Size and Quinary Structure Determine the Rheological Effects of Antibody Self-Association at High Concentrations. *J. Phys. Chem. B* **2018,** *122* (7), 2138-2154.
63. Wang, G.; Varga, Z.; Hofmann, J.; Zarraga, I. E.; Swan, J. W., Structure and Relaxation in Solutions of Monoclonal Antibodies. *J. Phys. Chem. B* **2018,** *122* (11), 2867-2880.
64. Chen, S. H., Small-angle neutron-scattering studies of the structure and interaction in micellar and microemulsion systems. *Annu. Rev. Phys. Chem.* **1986,** *37*, 351-399.
65. Lilyestrom, W. G.; Shire, S. J.; Scherer, T. M., Influence of the cosolute environment on IgG solution structure analyzed by small-angle X-ray scattering. *J. Phys. Chem. B* **2012,** *116* (32), 9611-8.
66. Kim, J. M.; Castaneda-Priego, R.; Liu, Y.; Wagner, N. J., On the importance of thermodynamic self-consistency for calculating clusterlike pair correlations in hard-core double Yukawa fluids. *The Journal of Chemical Physics* **2011,** *134* (6), 064904.
67. Plimpton, S., Fast Parallel Algorithms for Short-Range Molecular Dynamics. *Journal of Computational Physics* **1995,** *117* (1), 1-19.
68. Chandler, D.; Weeks, J. D.; Andersen, H. C., Van der Waals Picture of Liquids, Solids, and Phase Transformations. *Science* **1983,** *220* (4599), 787-794.
69. Laue, T., Proximity energies: a framework for understanding concentrated solutions. *J. Mol. Recognit.* **2012,** *25* (3), 165-73.
70. Riest, J.; Nagele, G.; Liu, Y.; Wagner, N. J.; Godfrin, P. D., Short-time dynamics of lysozyme solutions with competing short-range attraction and long-range repulsion: Experiment and theory. *J Chem Phys* **2018,** *148* (6), 065101.
71. Castellanos, M. M.; Howell, S. C.; Gallagher, D. T.; Curtis, J. E., Characterization of the NISTmAb reference material using small-angle scattering and molecular simulation. *Anal. Bioanal. Chem.* **2018**.
72. Dharmaraj, V. L.; Godfrin, P. D.; Liu, Y.; Hudson, S. D., Rheology of clustering protein solutions. *Biomicrofluidics* **2016,** *10* (4), 043509.
73. Yadav, S.; Scherer, T. M.; Shire, S. J.; Kalonia, D. S., Use of dynamic light scattering to determine second virial coefficient in a semidilute concentration regime. *Anal. Biochem.* **2011,** *411* (2), 292-6.
74. Holstein, M. A.; Parimal, S.; McCallum, S. A.; Cramer, S. M., Mobile phase modifier effects in multimodal cation exchange chromatography. *Biotechnol. Bioeng.* **2012,** *109* (1), 176-86.
75. Hou, Y.; Cramer, S. M., Evaluation of selectivity in multimodal anion exchange systems: A priori prediction of protein retention and examination of mobile phase modifier effects. *J Chromatogr A* **2011,** *1218* (43), 7813-20.
76. Arakawa, T.; Ejima, D.; Tsumoto, K.; Obeyama, N.; Tanaka, Y.; Kita, Y.; Timasheff, S. N., Suppression of Protein Interactions by Arginine: a Proposed Mechanism of the Arginine Effects. *Biophys. Chem.* **2007,** *127* (1-2), 1-8.
77. Shukla, D.; Trout, B. L., Interaction of Arginine with Proteins and the Mechanism by Which It Inhibits Aggregation. *J. Phys. Chem. B* **2010,** *114* (42), 13426-13438.
78. Shukla, D.; Schneider, C. P.; Trout, B. L., Molecular level insight into intra-solvent interaction effects on protein stability and aggregation. *Adv. Drug Deliv. Rev.* **2011,** *63* (13), 1074-85.
79. Bollinger, J. A.; Truskett, T. M., Fluids with competing interactions. I. Decoding the structure factor to detect and characterize self-limited clustering. *The Journal of Chemical Physics* **2016,** *145* (6), 064902.

80. Godfrin, P. D.; Valadez-Perez, N. E.; Castaneda-Priego, R.; Wagner, N. J.; Liu, Y., Generalized Phase Behavior of Cluster Formation in Colloidal Dispersions with Competing Interactions. *Soft Matter* **2014,** *10* (28), 5061-71.
81. Quang, L. J.; Sandler, S. I.; Lenhoff, A. M., Anisotropic contributions to protein-protein interactions. *J. Chem. Theory Comput.* **2014,** *10* (2), 835-45.
82. Smallenburg, F.; Sciortino, F., Liquids more stable than crystals in particles with limited valence and flexible bonds. *Nature Physics* **2013,** *9* (9), 554-558.

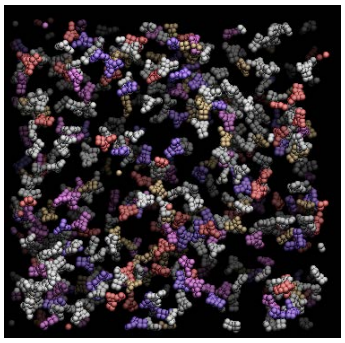

TOC Graphic